

Ageing-Aware Fast-Charging Strategy for Electric Vehicle Batteries

Increasing life expectancy of electric vehicle batteries by optimising fast charging strategies and thermal management for real-world conditions

Master's thesis in Complex Adaptive Systems

Olof Lind Stefansson
William Olsson

MASTER'S THESIS 2023

Ageing-Aware Fast-Charging Strategy for Electric Vehicle Batteries

Increasing life expectancy of electric vehicle batteries by optimising
fast charging strategies and thermal management for real-world
conditions

OLOF LIND STEFANSSON

WILLIAM OLSSON



CHALMERS
UNIVERSITY OF TECHNOLOGY

Department of Electrical Engineering
Division of Systems and Control
CHALMERS UNIVERSITY OF TECHNOLOGY
Gothenburg, Sweden 2023

Ageing-Aware Fast-Charging Strategy for Electric Vehicle Batteries
Increasing life expectancy of electric vehicle batteries by optimising fast charging
strategies and thermal management for real-world conditions
OLOF LIND STEFANSSON
WILLIAM OLSSON

© OLOF LIND STEFANSSON, 2023.
© WILLIAM OLSSON, 2023.

Supervisor: Chih Feng Lee, Project Manager and Developer, Polestar
Examiner: Changfu Zou, Associate Professor, Chalmers University of Technology

Master's Thesis 2023
Department of Electrical Engineering
Division of Systems and Control
Chalmers University of Technology
SE-412 96 Gothenburg
Telephone +46 31 772 1000

Typeset in L^AT_EX
Printed by Chalmers Reproservice
Gothenburg, Sweden 2023

Ageing-aware Fast-Charging Strategy for Electric Vehicle Batteries
Increasing life expectancy of electric vehicle batteries by optimising fast charging strategies and thermal management for real-world conditions
OLOF LIND STEFANSSON
WILLIAM OLSSON
Department of Electrical Engineering
Chalmers University of Technology

Abstract

Electric vehicles (EVs) are gaining popularity due to their reduced CO₂ emissions and climate impact compared to gasoline cars. However, lithium-ion batteries commonly used in EVs have environmentally harmful production and mining processes. To maintain battery performance throughout the warranty period, proper management is necessary, including maintenance, optimal charging, and temperature control. Faster charging requires charging protocols that optimise speed. Effective thermal management systems are also crucial to mitigate battery ageing caused by temperature and power variations during EV operation.

This thesis analysed factors that affect charging time and lithium-ion battery ageing in EVs. Its objective was to optimise a fast charging protocol, considering ambient and thermal conditions, as well as battery degradation. The degradation mechanisms that have been considered are lithium plating, solid electrolyte interface and particle cracking. The research focused on reducing charging times, extending battery lifespan, and developing an algorithm to handle charging and heating settings based on a given driving route. For the charging protocol optimisation it was found that a two-stage current protocol can reduce ageing compared to a one-stage current protocol. However, the study was limited to open source Python libraries for battery simulations. In addition, the battery models used were specifically designed for the simulation of individual battery cells.

Additionally it was found that the initial temperature of the battery before charge had a substantial impact on both charging speed and battery ageing. Two optimisation models were investigated, where the first approach considered optimising the thermal and charging at each phase of a journey separately, analogous to a well-tuned control system in production vehicles. The second approach considered the thermal and charging optimisation for the whole journey, where the fast charging phase is explicitly considered in the problem formulation. Our results showed that a considerable amount of time can be saved during charging by including the charging phase in the route planner.

Keywords: Battery ageing, Electric vehicles, Fast charge optimisation, Thermal management systems, Route planning, PyBaMM

Acknowledgements

We would like to express our deepest gratitude and appreciation to the following individuals who have significantly contributed to the completion of this master's thesis:

Our Supervisor, Chih Feng Lee:

We deeply appreciate your guidance, support, and expertise throughout our research journey. Your valuable insights and dedicated commitment have greatly shaped and enhanced the quality of this thesis.

Our Examiner and Supervisor, Changfu Zou:

We are grateful for your examination of this master's thesis. Your expertise, critical evaluation, and constructive feedback have greatly contributed to the refinement and improvement of our research. We sincerely appreciate your time and guidance.

Friends, and Family:

Our research journey has been made easier and more fulfilling due to the unwavering support of our family and friends. We are forever grateful for their love, understanding, and belief in our abilities.

Olof Lind Stefansson, Gothenburg, June 2023
William Olsson, Gothenburg, June 2023

List of Acronyms

Below is the list of acronyms that have been used throughout this thesis listed in alphabetical order:

CC-CV	Constant Current - Constant Voltage
DFN	Doyle-Fuller-Newman
EV	Electric Vehicle
MCC-CV	Multistage Constant Current - Constant Voltage
OCV	Open Circuit Voltage
PyBaMM	Python Battery Mathematical Modelling
SEI	Solid Electrolyte Interface
SoC	State of Charge
SPM	Single Particle model
SPMe	Single Particle Model with electrolyte
TMP	Thermal Management Protocol
TMS	Thermal Management System

Nomenclature

Below is the nomenclature of indices, sets, parameters, and variables that have been used throughout this thesis.

Indices

a	Air
b	Battery
$b2a$	Battery to air
$b2bc$	Battery to battery coolant
bc	Battery coolant
$bc2a$	Battery coolant to air
br	Battery resistance
chill	Chiller
cr	Crack
dis1	First discharge phase in a route
dis2	Second discharge phase in a route
e	Electrolyte
k	Index for location within each particle of active material. Can be separator or negative/positive part of cell
Li	Lithium
Li^+	Lithium ion
m_{cr}	Paris' law exponential term
s	Index for electrodes in battery (solid)
SEI	Solid electrolyte interface
t	Index for time step

Parameters

a_{\pm}	Surface area to volume ratio
$\alpha_{a,\text{Li}}$	Anodic transfer coefficient for Li stripping
$\alpha_{c,\text{Li}}$	Cathodic transfer coefficient for Li plating
b_{cr}	Stress intensity factor correction
c_p	Specific heat capacity
C_e	Ratio of electrolyte transport and discharge timescales
C_k	Ratio of solid diffusion and discharge timescales
\mathcal{D}_e	Electrolyte diffusivity
E	Young's modulus
ϵ_k	Electrolyte volume fraction
η_b	Battery propulsion efficiency
η_{b2bc}	Battery to battery coolant heat transfer efficiency
F	Faraday's constant
γ_0	Rate constant for dead Li formation
γ_e	Ratio of maximum lithium concentration in the negative electrode solid and typical electrolyte concentration
hA	Heat transfer coefficient
I	Total current density
$\hat{\kappa}$	Ratio of thermal voltage to the typical Ohmic drop in the electrolyte
k_{Li}	Li plating/stripping rate constant
k_{cr}	Paris' law cracking rate
L	Length
m	Mass
ν	Poisson's ratio
Ω	Partial molar volume
R	Universal gas constant
R_i	Particle radius
ρ_{cr}	Number of cracks per unit area
σ_k	Ratio of thermal voltage and typical Ohmic drop in the solid
t^+	Transference number
t_o	Time to complete one cycle
\bar{V}_{SEI}	SEI partial molar volume

w_{cr} Initial crack width

Variables

a Area
 b_{pwr} Battery power
 c Lithium ion concentration
 d Degradation
 D Diffusion coefficient
 η Over-potential
 ϕ Electric potential
 i Current density
 j Surface current density
 κ Conductivity
 mf Mass flow
 N Molar flux
 q Heat energy
 r 1D coordinate for location within each particle of active material
 σ Mechanical stress
 SoC State of charge
 t Time
 T Temperature
 U Voltage
 x 1D coordinate for location through thickness of battery



Contents

List of Acronyms	ix
Nomenclature	xi
List of Figures	xvii
List of Tables	xxi
1 Introduction	1
1.1 Background	1
1.2 Thesis Outline	2
1.3 Aim	3
1.4 Delimitations	3
2 Background	5
2.1 Lithium-Ion Batteries	5
2.1.1 Battery Degradation	6
2.1.1.1 SEI Growth	6
2.1.1.2 Lithium Plating	6
2.1.1.3 Particle Cracking	7
2.2 Lithium-Ion Battery Models	7
2.2.1 Electrochemical Battery Models	7
2.2.1.1 Doyle-Fuller-Newman Battery Model	8
2.2.1.2 Single Particle Model	9
2.2.1.3 Single Particle Model with Electrolyte	10
2.2.2 Battery Degradation Models	11
2.2.2.1 SEI Growth	11
2.2.2.2 Lithium Plating	12
2.2.2.3 Particle Cracking	12
2.2.3 Open Source Modelling Packages	13
2.3 Charging Protocols	14
3 Modelling and Charging Performance Analysis of Batteries	17
3.1 Battery Modelling	17
3.1.1 Comparison of Battery Models	17
3.1.2 SoC Definition	17
3.1.3 Thermal Model	18

3.2	Battery Model Properties	20
3.2.1	Correlations of Key Variables in Charging Process	20
3.2.2	Variables Controlling Charge Time	21
3.2.3	Contribution from Different Mechanisms	22
3.2.4	Long Term Degradation Behaviour	23
4	Enhancing Fast Charging Performance through Protocol Optimisation	25
4.1	Problem Formulation	25
4.1.1	Objective Function	25
4.2	Optimisation Algorithms	26
4.3	Feasible Operating Regions	27
4.4	Multistage Current Optimisation	29
4.4.1	Optimised Protocols	31
4.4.2	Long-Term Behaviour	31
5	Modelling of Battery Thermal Management During a Drive Cycle	35
5.1	Vehicle-Level Thermal Model Using Coolant Fluid	36
5.1.1	Parameter Tuning for Field Test Data	37
5.1.2	Model Hierarchy	39
5.1.2.1	Splitting Model Into Independent Sub-Models	40
5.1.2.2	Full Optimisation Model	40
5.2	Thermal Management Protocols	41
5.2.1	Protocols During Discharge	41
5.2.2	Protocols During Charge	41
5.2.2.1	Parameter Tuning for Usage in Charging Protocol with PyBaMM	43
6	Optimising Fast Charging Performance with Thermal Management	45
6.1	Chapter Overview	45
6.2	Phase-Wise Optimisation	45
6.2.1	Objective Function	45
6.2.2	Results From Phase-Wise Optimisation	46
6.3	Full Optimisation for the Complete Journey	48
6.3.1	Objective Function	48
6.3.2	Results From Full Optimisation	49
6.4	Comparison and modified objective function	50
7	Conclusion	55
7.1	Battery Modelling and Protocol Optimisation	55
7.2	Fast Charging with Thermal Management	56
7.3	Further Work	57
	Bibliography	59
	A Appendix 1	I

List of Figures

1.1	An outline of the thesis.	2
2.1	Illustration of a lithium-ion battery. The main components are the anode, cathode, separator and electrolyte. Lithium ions propagate through the separator and electrons are forced through an external wire during charge or discharge.	5
2.2	Illustration of how a SEI reaction occurs in a lithium-ion battery. The electrolyte on the anode surface participates in the reaction while the ions propagate between the electrodes during charging.	6
2.3	This illustration shows how lithium plating occurs in the battery during charging. While certain ions are involved in the process of intercalation within the electrode, others undergo a distinct transformation as they solidify into lithium on the surface of the anode.	7
2.4	Visualisation of the categories of approaches to estimating the state of charge in lithium-ion batteries. Taken from [1].	8
2.5	Examples of different charging strategies. a) Constant Current - Constant Voltage (CC-CV), b) Constant Power - Constant Voltage, c) Multistage Constant Current - Constant Voltage (MCC-CV), d) Pulse Charging, e) Boost Charging, f) Variable Current Profile (VCP). Images originated from [2]. This work considers CC-CV and MCC-CV.	14
3.1	A comparison of simulated terminal voltages using various battery models under different charge rates: (a) 1C and (b) 4C. The terminal voltage discrepancies of SPMe compared to DFN under different charge rates are also shown: (c) 1C and (d) 4C.	18
3.2	Illustration showing how the temperature changes in the lumped thermal model during a CC-CV protocol with C-rate 1.	19
3.3	Illustration of how the averaged temperature behaves during a CC-CV charge with an initial battery and ambient temperature of 20 °C. The initial SoC is 10 % and the target SoC is shown on the vertical axis.	19
3.4	The left diagram illustrates the voltage behaviour during CC-CV charging with different currents and ambient temperatures using SPMe. Using a C-rate of 3.5 in 0 °C shows a voltage spike exceeding the maximum limit. The right diagram shows how the voltage changes during charging with a C-rate of 3.5 in 0 °C with SPMe and DFN. DFN does not display the voltage spike, as shown by SPMe.	20

3.5	Correlation matrix showing the correlation of key variables during a CC-CV charge.	21
3.6	Charge time as a function of the target SoC and ambient temperature. There seems to be no difference in charge time at different ambient temperatures in the constant current part of the protocol. The constant voltage part of the protocol is however dependent on temperature where a lower temperature increases charge time.	22
3.7	Illustration of the degradation resulted from SEI, lithium plating and SEI on cracks during a CC-CV charge of a fresh battery.	23
3.8	Long term battery capacity loss due to SEI, lithium plating and SEI on cracks.	24
4.1	Definition of a charging protocol with a 3-stage current. The variables C_1, C_2, C_3 represent the current stages where C_1 is the first current applied. The variables SoC_1, SoC_2 indicate at what SoC the current switches.	26
4.2	Operating regions on a fresh battery where every point is an optimised CC-CV protocol using the objective function presented in (4.1). The x-axis represents the variable d_0 in (4.1), meaning the maximum allowed degradation.	27
4.3	Operating region on a seasoned battery where every point is an optimised CC-CV protocol using the objective function presented in (4.1). The horizontal axis represents the variable D in (4.1), meaning the maximum allowed degradation.	28
4.4	Comparison of capacity loss created with respect to the number of current stages and the desired charge time. There seems to be a benefit in terms of degradation from using a 2-stage current in the charging protocol. However, for the lowest possible charge times, multistage charging does not seem beneficial in terms of degradation.	30
4.5	Overview of the design of optimised MCC-CV protocols using 2-stage current. The left hand figure shows the SoC where the current switches. The middle figure indicates that the first current is always larger than the second. The right hand figure indicates that the second current is larger than the first one.	31
4.6	Long-term difference between a CC-CV protocol and an optimised two-stage current protocol with an ambient temperature of 5 °C. SEI and cracking seem to be lower for a CC-CV protocol but not for lithium plating which is dominant. This results in the two-stage current protocol generating less capacity loss overall.	32
4.7	Long term difference between a CC-CV protocol and an optimised two-stage current protocol with an ambient temperature of 35 °C. SEI and cracking seem to be similar for CC-CV and the two-stage current protocol but not for lithium plating which is smaller for the two-stage current protocol. This results in the two-stage current protocol generating lower capacity loss overall.	32

5.1	Overview of the route. The vehicle starts driving from point A with TMP active. The vehicle is then charged with a charging protocol at a fast charging station and also uses a TMP. Finally the vehicle drives to its end destination at point B while another TMP is active.	35
5.2	Visualisation of the TMS used in an EV. The blue line represents the coolant fluid in the vehicle.	36
5.3	Illustration of the results from the parameter tuning of parameters A-D in (5.3) using a set of training routes. Routes A-B and E-F seem to have slightly higher relative error than the others. Their battery temperatures also seem lower compared to the others. The different route locations have been encoded to letters since these are confidential.	38
5.4	Illustration of how the tuned parameters A-D performed on the test dataset. Results seem to be of similar quality to those of the training data in figure 5.3. The different route locations have been encoded into letters since they are confidential. Each letter corresponds to a location.	39
5.5	Illustration of the absolute error distribution while comparing the tuned thermal model to field test data. As shown in the left image, the data has been categorised by route, with each letter representing a location. The right image shows a histogram where the data is categorised by 5 °C intervals spanning from the lowest possible temperature (interval 1) to the highest possible temperature (interval 7).	40
5.6	Visualisation of the optimisation for the sub-optimisation model. Every phase is optimised independently where every sub model uses fewer parameters than the entire model resulting in faster optimisation convergence.	41
5.7	Visualisation of the full optimisation model. The model runs through the entire route and evaluates the objective function.	41
5.8	The definition of a thermal management protocol (TMP). In (5.3), the power of the TMP is expressed as q_{chill}	42
5.9	Illustration of a TMP during charging in PyBaMM. The reference coolant temperature is controlled through Heaviside's step functions. It changes from 20 to -5 °C after 10 seconds and from -5 to -20 °C after 30 seconds.	42
5.10	Illustration of the results of the parameter tuning of the surface heat transfer coefficient in PyBaMM using a set of training routes. Routes A-B and E-F seem to have slightly higher relative error than the others. Their battery temperatures also seems to be slightly lower compared to the others. This error-temperature trend is similar to the one illustrated in figure 5.3. The different route locations have been encoded to letters since these are confidential. Each letter A-I corresponds to a location.	43
5.11	Illustration of how the tuned surface heat transfer coefficient from PyBaMM performed on the test dataset. Results seem to be of similar quality to the results from the training data in figure 5.10.	44

6.1	Illustration of optimised protocols for cold ambient temperature with phase-wise optimisation and target temperature penalty. Heating is needed to keep the temperature of the battery close to the target temperature. Battery is close to empty when it reaches its destination.	47
6.2	Illustration of optimised protocols for warm ambient temperature with phase-wise optimisation and with target temperature penalty. Since the ambient temperature is considerably warmer than the ambient temperature in figure 6.1, cooling has to be done to keep the temperature of the battery close to the target temperature. Battery is close to empty when it reaches its destination.	48
6.3	Illustration of optimised protocols for cold ambient temperature with full optimisation and the target temperature penalty. Heating is needed to maintain the target temperature. Battery is close to empty when it reaches the destination.	49
6.4	Illustration of optimised protocols for a warm ambient temperature with full optimisation and the target temperature penalty. Since the ambient temperature is considerably warmer than the ambient temperature in figure 6.3, cooling has to be done to keep the battery temperature close to the target temperature. SoC is almost empty when it reaches its destination.	50
6.5	Illustration of optimised protocols for warm ambient temperatures with phase-wise optimisation and the target temperature penalty. Since the ambient temperature is warm, cooling is needed to keep the battery temperature close to the target temperature. At the end of the journey, SoC is 50%.	51
6.6	Illustration of optimised protocols for warm ambient temperatures with phase-wise optimisation and without the target temperature penalty. The objective function is simplified so that it is only concerned with minimising energy in the discharge phase and the charge time in the charge phase. The SoC is 50% when the EV reaches its destination.	52
6.7	Illustration of optimised protocols for a warm ambient temperature with full optimisation and without the target temperature penalty. The objective function is simplified so as to minimise the total travel time. When the EV reaches its destination, the SoC is 50%.	52
A.1	Operating region for PyBaMM. Numerical instability was observed when simulating charging at high current in cold environments using PyBaMM. During charging, the temperature is fixed in this simulation using a non-isothermal model. If an isothermal model were used, the boundary would be pushed to higher temperatures.	II

List of Tables

5.1	Summary of the field test data.	38
A.1	Table of the two-stage charge protocol with respect to charging time and ambient temperature. The variables C_1, SoC_1, C_2 are described in figure 4.1.	I

1

Introduction

1.1 Background

Electric vehicles (EVs) have over the last few years seen a massive increase. They emit significantly less carbon dioxide and do not contribute to global warming or climate change nearly as much as gasoline-driven cars [3]. Car manufacturers are transitioning to fully electric cars [4]. The energy required from the vehicles is stored in battery packs and supplies the vehicle with electricity when needed.

The most common EV battery type is lithium-ion batteries, due to their high energy density and fast charging capabilities. Even though lithium batteries are more environmentally friendly than traditional combustion vehicles, lithium mining disrupts ecosystems and contributes to global warming [5]. Customers using products containing these types of batteries also have expectations about how long their product should last in terms of quality. Most EVs produced today have the warranty that the battery should last for 100,000 to 200,000 miles [6]. It is therefore crucial to engage the battery in ways that slow down the degradation of its capacity or performance. Implementing proper battery management practices, such as regular maintenance, optimal charging habits, and temperature control, can preserve battery longevity. This will ensure it meets or exceeds the warranty period.

Battery degradation is partially caused by battery charging. Aggressive battery charging can cause different degradation phenomena making the battery lose a substantial part of its total capacity and maximum power output. Meanwhile EV owners want fast charge times and small queues at charging stations [7]. Therefore, it is of high interest to find a charging protocol that recharges the battery fast while decelerating battery degradation. An article in Nature emphasised the importance of using the right charging protocol. It also emphasised that the lifespan can vary a lot depending on how their battery was charged [8]. Some of their protocols were generated using optimisation techniques and outperformed literature-inspired protocols. While driving an EV the surrounding conditions in terms of temperature and power demand from the electric motor can vary a lot. These parameters play a significant role in the ageing process of the battery. The way it is charged under these conditions can cause considerable variation in the battery's lifespan. Other studies have shown that an effective battery thermal management system (TMS) is essential for maintaining the optimal operating temperature of lithium-ion batteries in EVs, preserving their desirable characteristics in terms of battery ageing [9].

1.2 Thesis Outline

This thesis is structured into an introduction that presents and motivates the thesis's purpose. The introduction is then followed by a background chapter where necessary theory is presented, mostly on battery models and battery degradation mechanisms. The background chapter also covers contributions and previous work that is relevant. The remainder of the thesis is divided into two parts. The first part consists of two chapters, starting with battery modelling and analysis, and followed by fast charging protocol optimisation. The second part consists of two chapters, where the battery thermal system is modelled, followed by optimising fast charging performance considering battery thermal management. The thesis structure is illustrated in figure 1.1.

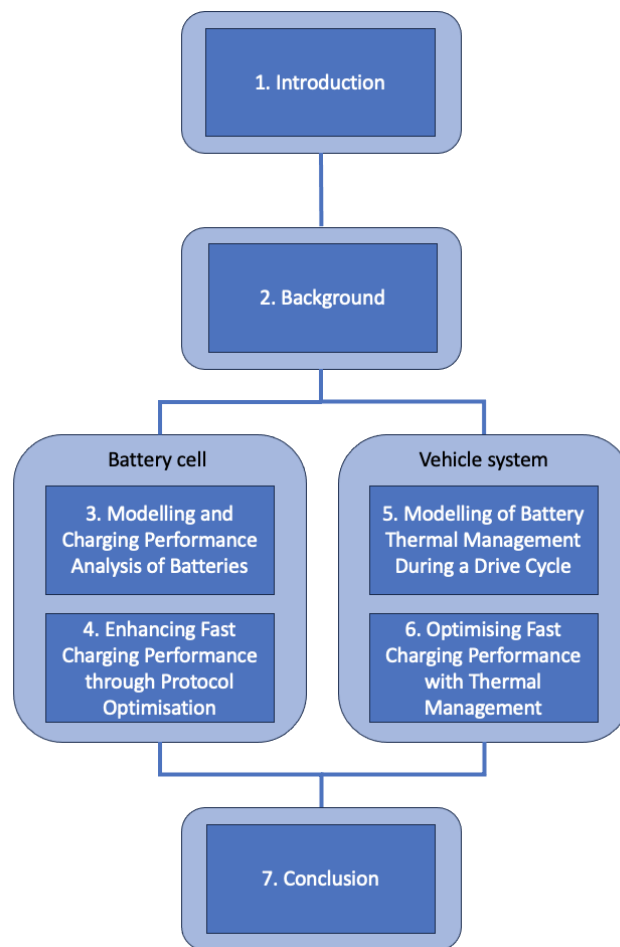


Figure 1.1: An outline of the thesis.

1.3 Aim

The objective of this thesis is to understand and improve the charge time of lithium-ion batteries considering battery ageing. The research questions are formulated as the following:

1. What factors affect charge time and ageing of lithium batteries?
2. How can fast charging performance be improved under realistic real-world operating conditions?

We will first explore the modelling of battery cells, and the model will then be used to optimise fast charging protocols. In order to improve fast charging performance under real-world driving conditions, battery energy and thermal behaviour is examined and modelled. As a result, the thermal and charging protocols are optimised under predefined routes.

1.4 Delimitations

One limitation of this thesis is that all simulations regarding the battery are done in the open source python package PyBaMM. Although data has been used in the development of PyBaMM, data to validate battery models in an EV setting has not been available during this thesis. Besides, all battery models used in this thesis are electrochemical models designed for one cell lithium ion batteries.

2

Background

2.1 Lithium-Ion Batteries

The main components in a lithium ion battery are the anode, cathode and separator. The anode and cathode are electrodes where the anode is the negative charged part and the cathode is the positive. Lithium metal oxide is commonly used as cathode material as it stabilises lithium. The anode is often made of graphite as it stores energy efficiently. The separator is located between the two electrodes and its function is to prevent electrons from travelling through the separator. Figure 2.1 shows a visualisation of a lithium battery. The way lithium-ion batteries are

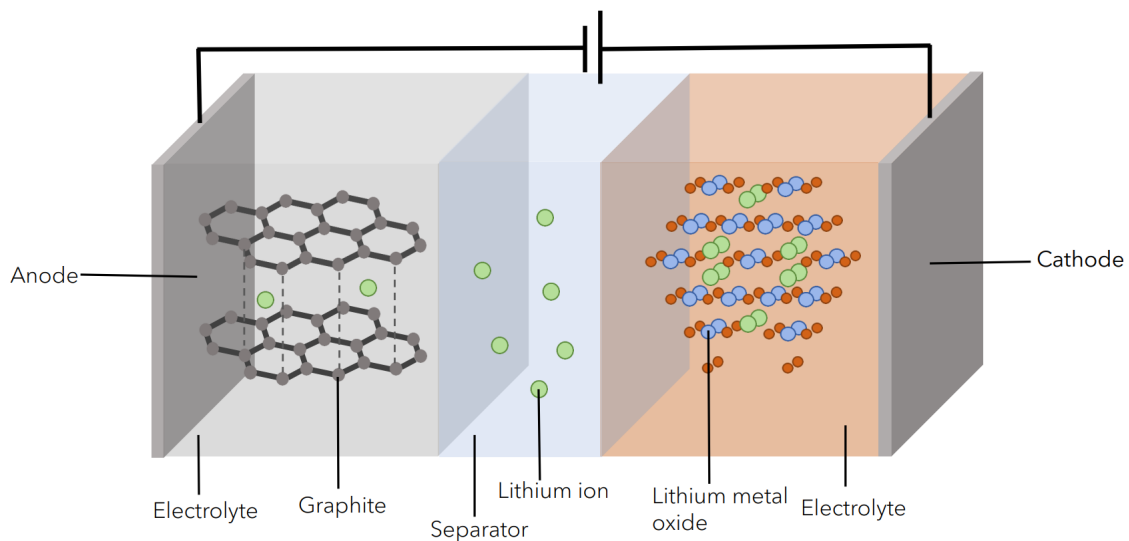


Figure 2.1: Illustration of a lithium-ion battery. The main components are the anode, cathode, separator and electrolyte. Lithium ions propagate through the separator and electrons are forced through an external wire during charge or discharge.

used to store and output energy is by transporting lithium ions. A power supply is applied over the battery during charging to force lithium ions from the anode to the cathode through the separator. Electrons cannot bypass the separator and are forced to move around the battery creating a current that can be used for external work. Upon passing the external wire, the electrons are reunited with lithium ions, forming lithium atoms. The cathode intercalates lithium atoms during this process.

A key component in the battery in fast charging settings is the electrolyte. Dif-

ferent battery manufacturers use different electrolytes of different viscosity in their lithium-ion batteries. The purpose of the electrolyte is to enhance the transport capability of lithium ions. Because of this, the choice of electrolyte in the electrodes is particularly important in fast charging scenarios [10]. This chapter introduces several new variables, all variables are introduced in the nomenclature list.

2.1.1 Battery Degradation

Battery performance and lifespan are affected by a variety of factors, such as temperature, charging and discharge rates, and chemical reactions inside the battery. This section describes three mechanisms: lithium plating, SEI growth and particle cracking.

2.1.1.1 SEI Growth

Electrolytes used in lithium-ion batteries are stable when the potential difference compared to the Li/Li^+ is larger than 1 V [11]. But the potential difference is usually much smaller than this, making the electrolyte in the cell unstable. This causes a reaction with the lithiated graphite electrode that creates a solid electrolyte interface (SEI) layer on the electrode. As a result of this reaction some of the lithium that reacts with the electrolyte gets trapped in the SEI layer. This means that less lithium can take part in the charge and discharge reaction and therefore implies a reduced battery capacity [11]. Figure 2.2 illustrates how the SEI growth

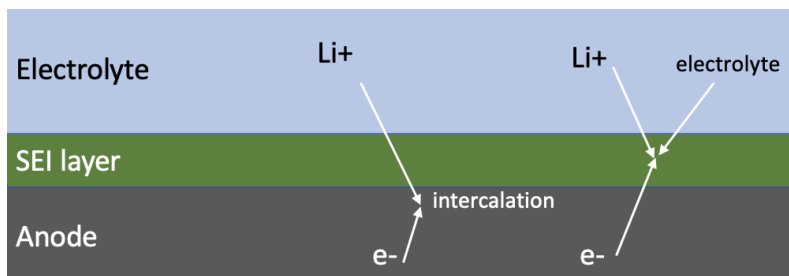


Figure 2.2: Illustration of how a SEI reaction occurs in a lithium-ion battery. The electrolyte on the anode surface participates in the reaction while the ions propagate between the electrodes during charging.

reaction occurs in a battery. While the ions propagate between the electrodes during charging, the reactive electrolyte participates in the reaction and forms a layer on the anode surface.

2.1.1.2 Lithium Plating

Lithium plating is another degradation mechanism where solid lithium metal is accumulated on the surface of the graphite electrode. As opposed to intercalating into graphite. The mechanism has been the focus of in-depth reviews [12, 13] where the conclusion was that the main triggers for the mechanism are low temperatures and fast charging. Electroplating reactions usually have a reversible process and

in this case it is commonly known as lithium stripping. This is where the plated lithium oxidises and returns the ions to the electrolyte [11]. Although the plating is reversible, SEI growth can cover the plated lithium causing irreversible plating formation, also known as dead lithium. Figure 2.3 shows how lithium plating occurs

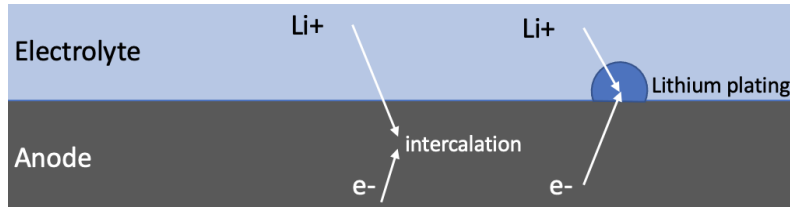


Figure 2.3: This illustration shows how lithium plating occurs in the battery during charging. While certain ions are involved in the process of intercalation within the electrode, others undergo a distinct transformation as they solidify into lithium on the surface of the anode.

in the battery during charging. While some ions intercalate in the electrode, others form solid lithium on the anode surface.

2.1.1.3 Particle Cracking

During battery cycling, the volume of the electrode changes. Delithiation causes contractions and expansions on lithiation [14]. This results in mechanical stress within the electrodes that can result in particle cracking. Previous studies have shown that one of the main triggers of particle cracking is high currents [15]. In terms of degradation this mechanism causes the surface area to increase which increases the probability of SEI growth [16], which similar to previous mechanisms causes less lithium to take part in the charging/discharging reaction and reduces the capacity.

2.2 Lithium-Ion Battery Models

There are different ways of modelling a battery. The options for state of charge (SoC) estimation are illustrated in figure 2.4. For example, there are electric circuit models, data driven models and electrochemical models, which all have different advantages and drawbacks. This work will focus on electrochemical models as they provide higher accuracy than traditional electrical circuit models [17]. Electrochemical models also give an insight into the internal dynamics of the battery, which is useful when evaluating degradation mechanisms. We present three electrochemical models, the Doyle-Fuller-Newman (DFN) model, Single Particle model (SPM) and Single Particle model with electrolyte (SPMe). This section introduces several new variables, all variables are introduced in the nomenclature list.

2.2.1 Electrochemical Battery Models

Mathematical models of batteries are necessary to fully understand their behaviour. The internal process of battery degradation is mostly a chemical process and electrochemical models are necessary to model mechanisms.

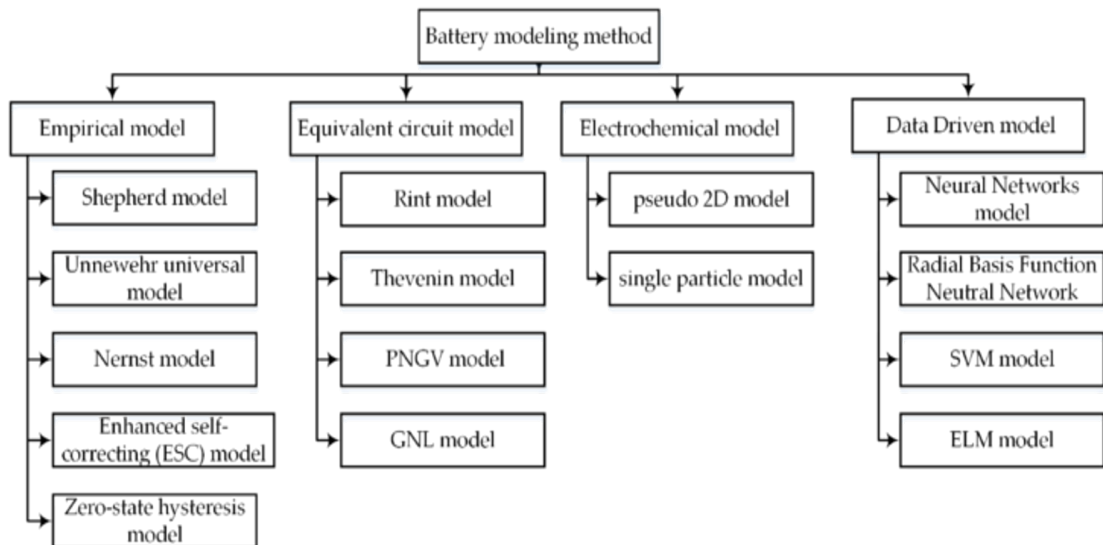


Figure 2.4: Visualisation of the categories of approaches to estimating the state of charge in lithium-ion batteries. Taken from [1].

The standard model for modelling lithium-ion batteries is the DFN model [18]. The model consists of partial differential equations that are fairly complex and computationally time-consuming. Other models such as the SPM are less complex but can lead to higher errors when high currents are applied [18]. The paper by Marquis [18] involves derivations of these models and presents an extended SPM model to model the electrolytes accurately. As a result, it will be more accurate than SPM and less complex than DFN at displaying battery behaviour. This model is called SPMe.

2.2.1.1 Doyle-Fuller-Newman Battery Model

The Doyle-Fuller-Newman (DFN) battery model has become a standard in mathematical battery modelling [19]. The DFN model is derived using volume averaging or "The Method of Multiple Scales". The DFN model is described as a set of partial differential equations that are highly coupled. Each equation is connected to a conservation law. The different conservation laws in an electrochemical battery model are charge, mass and electrochemical conservation. Equation (2.1) shows the governing equations describing the DFN model.

Charge conservation:

$$\begin{aligned}
 \frac{\partial i_{e,k}}{\partial x} &= \begin{cases} j_k, & k = n, p \\ 0, & k = s \end{cases} \\
 C_e i_{e,k} &= \epsilon_k^b \hat{\kappa}_e \kappa_e (c_{e,k}) \left(-\frac{\partial \phi_{e,k}}{\partial x} + 2(1-t^+) \frac{\partial}{\partial x} (\log(c_{e,k})) \right), \\
 I - i_{e,k} &= -\sigma_k \frac{\partial \phi_{s,k}}{\partial x}, \quad k \in \{n, s, p\}
 \end{aligned} \tag{2.1}$$

Mass conservation:

$$\begin{aligned} \mathcal{C}_e \epsilon_k \gamma_e \frac{\partial c_{e,k}}{\partial t} &= -\gamma_e \frac{\partial N_{e,k}}{\partial x} + \mathcal{C}_e \frac{\partial i_{e,k}}{\partial x}, & k \in \{n, s, p\} \\ N_{e,k} &= -\epsilon_k^b D_e(c_{e,k}) \frac{\partial c_{e,k}}{\partial x} + \frac{\mathcal{C}_e t^+}{\gamma_e} i_{e,k}, & k \in \{n, s, p\} \\ \mathcal{C}_k \frac{\partial c_{s,k}}{\partial t} &= -\frac{1}{r_k^2} \frac{\partial}{\partial r_k} \left(r_k^2 \frac{\partial c_{s,k}}{\partial r_k} \right), & k \in \{n, p\} \end{aligned}$$

Electrochemical reactions:

$$\begin{aligned} j_k &= 2j_{0,k} \sinh\left(\frac{\eta_k}{2}\right), & k \in \{n, p\} \\ j_{0,k} &= \frac{\gamma_k}{\mathcal{C}_{r,k}} c_{s,k}^{1/2} (1 - c_{s,k})^{1/2} c_{e,k}^{1/2} \Big|_{r_k=1}, & k \in \{n, p\} \\ \eta_k &= \phi_{s,k} - \phi_{e,k} - U_k(c_{s,k}|_{r_k=1}), & k \in \{n, p\} \end{aligned}$$

Voltage expression

$$U = \phi_{s,p}|_{x=1} - \phi_{s,n}|_{x=0}$$

The DFN model has shown itself to be computationally heavy and memory demanding. The DFN model is often too resource demanding and not used in most industrial applications [18]. It is common to make assumptions to simplify internal battery dynamics.

2.2.1.2 Single Particle Model

The SPM is a more simplistic electrochemical battery model than DFN. It is derived from the DFN model with two assumptions. The first assumption is that the electrical conductivity in the electrodes and electrolyte is large. The second assumption is that lithium ion migration timescale is considerably larger than the discharge timescale. Using these assumptions, one can expand all relevant variables using the ratio of the lithium ion migration timescale and the discharge capacity timescale.

$$v = v^0 + v^1 \mathbf{C}_e + v^2 \mathbf{C}_e^2 \dots \quad (2.2)$$

Equation (2.2) describes the expansion in the term \mathbf{C}_e which is the ratio of the lithium ion migration timescale and the discharge timescale. In the limit $\mathbf{C}_e \rightarrow 0$, only the term v_0 remains in the equation and is usually called the leading order. Using the leading order approximation simplifies the DFN model into the SPM model and is summarised in (2.3).

$$\begin{aligned}
 \mathcal{C}_k \frac{\partial c_{s,k}^0}{\partial t} &= \frac{1}{r_k^2} \frac{\partial}{\partial r_k} \left(r_k^2 \frac{\partial c_{s,k}^0}{\partial r_k} \right), \quad k \in \{n, p\} \\
 \frac{\partial c_{s,k}^0}{\partial r_k} \Big|_{r_k=0} &= 0 \quad k \in \{n, p\} \\
 - \frac{a_k \gamma_k}{\mathcal{C}_k} \frac{\partial c_{s,k}^0}{\partial r_k} \Big|_{r_k=1} &= \begin{cases} \frac{I}{L_n}, & k = n, \\ -\frac{I}{L_p}, & k = p, \end{cases} \quad k \in \{n, p\} \\
 c_{s,k}^0(r_k, 0) &= c_{s,k,0}, \quad k \in \{n, p\}
 \end{aligned} \tag{2.3}$$

Equation (2.3) describes the governing equations in SPM dynamics. Notice that there is no effect from the electrolyte as in (2.1). As a final remark, the name single particle model indicates that there is only one active material particle. The single particle model has its name because each active material particle behaves equally, meaning that analysing one particle is enough to understand the whole system. The SPM model voltage expression is given in (2.4).

$$\begin{aligned}
 U &= \underbrace{U_p(c_{s,p}^0) \Big|_{r_p=1} - U_n(c_{s,n}^0) \Big|_{r_n=1}}_{\text{OCV}} - \underbrace{2 \sinh^{-1} \left(\frac{I}{j_{0,p} L_p} \right) - 2 \sinh^{-1} \left(\frac{I}{j_{0,n} L_n} \right)}_{\text{Reaction over-potentials}} \\
 j_{0,k} &= \frac{\gamma_k}{\mathcal{C}_{r,k}} (c_k^0)^{1/2} (1 - c_k)^{1/2}
 \end{aligned} \tag{2.4}$$

2.2.1.3 Single Particle Model with Electrolyte

SPMe is an extension of the SPM model. In (2.2), its dynamics are derived by including the second term v_1 . An critical step in deriving the SPMe model dynamics is electrode averaging. Its dynamics are described in (2.5).

$$\begin{aligned}
 \mathcal{C}_k \frac{\partial c_{s,k}}{\partial t} &= -\frac{1}{r_k^2} \frac{\partial}{\partial r_k} \left(r_k^2 N_{s,k} \right) \quad k \in \{n, p\} \\
 N_{s,k} &= -D_{s,k}(c_{s,k}) \frac{\partial c_{s,k}}{\partial r_k} \quad k \in \{n, p\} \\
 N_{s,k} \Big|_{r_k=0} &= 0 \quad k \in \{n, p\} \\
 - \frac{a_{R,k} \gamma_k}{\mathcal{C}_k} N_{s,k} \Big|_{r_k=1} &= \begin{cases} \frac{I}{L_n}, & k = n, \\ \frac{I}{L_p}, & k = p, \end{cases} \quad k \in \{n, p\} \\
 c_{s,k}(r_k, 0) &= c_{s,k,0} \quad k \in \{n, p\}
 \end{aligned} \tag{2.5}$$

The dynamics from (2.5) shows that SPMe has the same dynamics as SPM with some extensions from the electrolyte. The voltage expression for the SPMe model

is given in (2.6).

$$\begin{aligned}
 U &= \underbrace{\bar{U}_{\text{eq}}}_{\text{OCV}} + \underbrace{\bar{\eta}_r}_{\text{reaction over-potential}} + \underbrace{\bar{\eta}_c}_{\text{concentration over-potential}} + \underbrace{\overline{\Delta\Phi}_{\text{Elec}} + \overline{\Delta\Phi}_{\text{Solid}}}_{\text{Ohmic losses}} \\
 \bar{U}_{\text{eq}} &= U_{\text{p}}(c_{\text{s,p}}^0)|_{r_{\text{p}}=1} - U_{\text{n}}(c_{\text{s,n}}^0)|_{r_{\text{n}}=1} \\
 \bar{\eta}_r &= -2 \sinh^{-1} \left(\frac{I}{\bar{j}_{0,\text{p}} L_{\text{p}}} \right) - 2 \sinh^{-1} \left(\frac{I}{\bar{j}_{0,\text{n}} L_{\text{n}}} \right) \\
 \bar{\eta}_c &= 2\mathcal{C}_e (1 - t^+) (\bar{c}_{\text{e,p}}^1 - \bar{c}_{\text{e,n}}^1) \\
 \bar{j}_{0,\text{n}} &= \frac{1}{L_{\text{n}}} \int_0^{L_{\text{n}}} \frac{\gamma_{\text{n}}}{\mathcal{C}_{\text{r,n}}} (c_{\text{s,n}}^0)^{1/2} (1 - c_{\text{s,n}}^0)^{1/2} (1 + \mathcal{C}_e c_{\text{e,n}}^1)^{1/2} dx \\
 \bar{j}_{0,\text{p}} &= \frac{1}{L_{\text{p}}} \int_{1-L_{\text{p}}}^1 \frac{\gamma_{\text{p}}}{\mathcal{C}_{\text{r,p}}} (c_{\text{s,p}}^0)^{1/2} (1 - c_{\text{s,p}}^0)^{1/2} (1 + \mathcal{C}_e c_{\text{e,p}}^1)^{1/2} dx \\
 \overline{\Delta\Phi}_{\text{Elec}} &= -\frac{I}{\hat{\kappa}_e \kappa_e (1)} \left(\frac{L_{\text{n}}}{3\epsilon_{\text{n}}^b} + \frac{L_{\text{s}}}{\epsilon_{\text{s}}^b} + \frac{L_{\text{p}}}{3\epsilon_{\text{p}}^b} \right) \\
 \overline{\Delta\Phi}_{\text{Solid}} &= -\frac{I}{3} \left(\frac{L_{\text{p}}}{\sigma_{\text{p}}} + \frac{L_{\text{n}}}{\sigma_{\text{n}}} \right)
 \end{aligned} \tag{2.6}$$

2.2.2 Battery Degradation Models

This section will describe the different degradation model used for each mechanism and how these models sometimes interact with each other.

2.2.2.1 SEI Growth

The model used in Safari *et al.* [20] has become the foundation of most SEI models in the recent literature. In their study, they found that two factors limit the main SEI reaction involving Li+ and an organic solvent. In order to reach the graphite surface, solvent molecules must first diffuse through the SEI. The graphite must then provide an electron to reduce the solvent molecules. The model accounts for both limitations, but it provides the most accurate fit to experimental data when growth is limited by diffusion. This part is governed by Fick's diffusion law.

$$\begin{aligned}
 N_{\text{e}} &= -D_{\text{e}}(T) \frac{\partial c_{\text{e}}}{\partial x} \\
 c_{\text{e}} &= 0 \quad \text{at} \quad x = 0, \\
 c_{\text{e}} &= c_{\text{e},0} \quad \text{at} \quad x = L_{\text{SEI}}
 \end{aligned} \tag{2.7}$$

The solution to this equation is given by

$$c_{\text{e}} = \frac{x c_{\text{e},0}}{L_{\text{SEI}}} \quad \text{and} \quad N_{\text{e}} = -\frac{c_{\text{e},0} D_{\text{e}}(T)}{L_{\text{SEI}}}. \tag{2.8}$$

The SEI layers inter-facial flux density is a result of mass conservation and is given by

$$N_{\text{SEI}} = -N_{\text{e}}, \tag{2.9}$$

where the SEI layered growth is given by

$$\frac{\partial L_{\text{SEI}}}{\partial t} = -\frac{1}{2}N_e\bar{U}_{\text{SEI}} = \frac{c_{e,0}D_e(T)\bar{V}_{\text{SEI}}}{2L_{\text{SEI}}}. \quad (2.10)$$

2.2.2.2 Lithium Plating

In this work, Wood *et al.*'s [21] lithium plating model have been adopted, where the flux of lithium ions in the battery is described by

$$N_{\text{Li}} = k_{\text{Li}} \left(c_{\text{Li}} \exp\left(\frac{F\alpha_{a,\text{Li}}\eta_{\text{Li}}}{RT}\right) - c_e \exp\left(-\frac{F\alpha_{c,\text{Li}}\eta_{\text{Li}}}{RT}\right) \right). \quad (2.11)$$

Equation (2.11) is an extension of the Butler-Volmer equation. The Butler-Volmer equation is a well-known electrochemistry equation. It contains some minor adjustments by O'Kane [11] to account for the coupled reactions between SEI, plating and dead lithium using

$$\eta_{\text{Li}} = \phi_s - \phi_e - \eta_{\text{SEI}}, \quad (2.12)$$

where η_{Li} refers to the lithium over-potential. The lithium over-potential is a vital variable in lithium plating modelling. The key to slowing ageing from a lithium plating standpoint is to keep the lithium over-potential above 0. When $\eta_{\text{Li}} < 0$ the second term in (2.11) is positive resulting in a loss of available lithium in the battery. O'Kane presents a model that accounts for both lithium plating, lithium stripping and dead lithium based on this equation [11]. The governing equation for lithium concentration in battery cells is given by

$$\frac{\partial c_{\text{Li}}}{\partial t} = -a_- N_{\text{Li}} - \gamma c_{\text{Li}}. \quad (2.13)$$

The first term accounts for the separation of electrons and lithium ions due to expected reactions. c_{dl} accounts for the dead lithium growth rate given by

$$\frac{\partial c_{\text{dl}}}{\partial t} = \gamma c_{\text{Li}}. \quad (2.14)$$

The value of γ is inversely proportional to the SEI layer thickness. The explicit equation can be found in the following equation.

$$\gamma(L_{\text{SEI}}) = \gamma_0 \frac{L_{\text{SEI},0}}{L_{\text{SEI}}} \quad (2.15)$$

2.2.2.3 Particle Cracking

The particle cracking model is based on the physics-based model introduced in O'Kane's paper [11], which will be described in this section. Particle cracking accelerates SEI growth and Li plating. Existing crack models for battery degradation are either empirical or physics-based. The fatigue crack model by Deshpande et al. [22] and the stress model by Zhang et al. [23] are employed. Equations for radial stress (σ_r), tangential stress (σ_t), and displacement (u) are derived.

$$\begin{aligned}
 \sigma_r &= \frac{2\Omega E}{(1-\nu)} [c_{\text{avg}}(R_i) - c_{\text{avg}}(r)] \\
 \sigma_t &= \frac{\Omega E}{(1-\nu)} [2c_{\text{avg}}(R_i) + c_{\text{avg}}(r) - \bar{c}/3] \\
 u &= \frac{(1+\nu)}{(1-\nu)} \Omega r c_{\text{avg}}(r) + \frac{2(1-2\nu)}{(1-\nu)} \Omega r c_{\text{avg}}(R_i)
 \end{aligned} \tag{2.16}$$

Here, Ω represents the partial molar volume, E is Young's modulus, ν is Poisson's ratio, R_i is the particle radius, and c_{avg} is the average lithium-ion concentration.

Electrode particles undergo cyclic stress loading during charge and discharge cycles, leading to fatigue cracking. Tracking crack patterns experimentally is challenging. Using Deshpande et al.'s [22] crack assumptions and Paris' law, this study models fatigue crack growth through the following expression where x_{cr} represents crack length.

$$\frac{dx_{\text{cr}}}{dN} = \frac{k_{\text{cr}}}{t_0} (\sigma_t b_{\text{cr}} \sqrt{\pi x_{\text{cr}}})^{m_{\text{cr}}} \quad \sigma_t > 0. \tag{2.17}$$

In this context, t_0 represents the time required for one complete cycle, b_{cr} denotes the stress intensity factor correction, and k_{cr} and m_{cr} are constants derived from experimental data, such as the methodology employed by Purewal et al. [24].

The instantaneous rate of change in crack area to volume ratio is estimated by

$$\frac{da_{\text{cr}}}{dt} = \frac{a_{\pm} \rho_{\text{cr}} w_{\text{cr}}}{t_0} \cdot \frac{dx_{\text{cr}}}{dt} = \frac{a_{\pm} \rho_{\text{cr}} w_{\text{cr}}}{t_0} \cdot k_{\text{cr}} (\sigma_t b_{\text{cr}} \sqrt{\pi x_{\text{cr}}})^{m_{\text{cr}}} \quad \sigma_t > 0, \tag{2.18}$$

where w_{cr} is crack width and ρ_{cr} is crack density per unit area.

To account for the interaction between SEI growth and particle cracking, a model is proposed where SEI growth is applied to cracks separately.

$$\frac{\partial L_{\text{SEI,cr}}}{\partial t} = \frac{c_{e,0} D_e(T) \bar{V}_{\text{SEI}}}{2L_{\text{SEI,cr}}} + \frac{\partial x_{\text{cr}}}{\partial t} \frac{L_{\text{SEI,cr0}} - L_{\text{SEI,cr}}}{x_{\text{cr}}} \tag{2.19}$$

SEI layer thickness evolves over time, considering diffusion-limited growth in existing cracks and reduction due to crack propagation.

2.2.3 Open Source Modelling Packages

One tool for modelling batteries is PyBaMM (Python Battery Mathematical Model) [25]. It is an open-source library that provides tools for modelling different types of batteries including lithium-ion batteries. It supports models such as SPM, SPMe and DFN and also provides parameter sets from previously conducted studies in the field. The modular design of the software makes it possible to use different sub-models as building blocks. This makes it possible to include or exclude relevant degradation mechanisms or other necessary aspects of simulations. It has separate building blocks for mechanisms such as SEI growth, lithium plating and particle cracking.

2.3 Charging Protocols

A charging protocol is a set of rules and standards that govern how a battery is charged. The charging protocol specifies the electrical and communication requirements between the charger and the device being charged. This step ensures the charging process is safe, efficient, and effective. Charging protocols ensure devices are charged properly. This can extend the battery's life, prevent overheating or other safety issues, and make sure that the device is charged as quickly as possible [26]. In more detail, a charging protocol is a predetermined way to control the current density while charging the battery. The current density can be controlled in several ways, for example by keeping the voltage, charge current or power delivery constant [2].

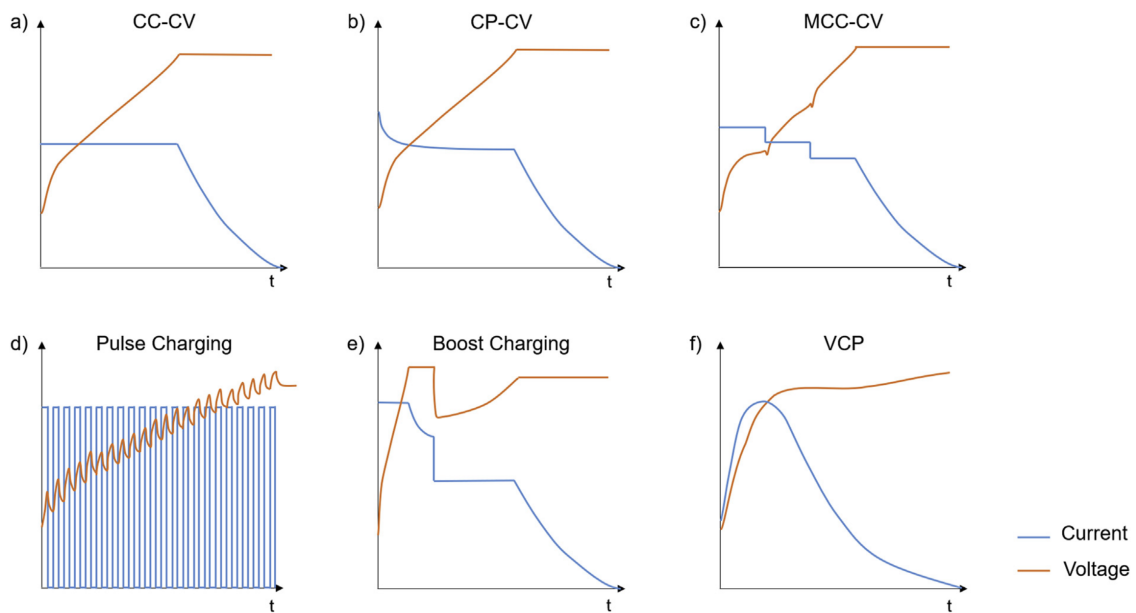


Figure 2.5: Examples of different charging strategies. a) Constant Current - Constant Voltage (CC-CV), b) Constant Power - Constant Voltage, c) Multistage Constant Current - Constant Voltage (MCC-CV), d) Pulse Charging, e) Boost Charging, f) Variable Current Profile (VCP). Images originated from [2]. This work considers CC-CV and MCC-CV.

The most common charging protocols are presented in figure 2.5. A Constant Current - Constant Voltage (CC-CV) protocol starts with a constant current until it reaches a certain voltage level, typically 70 to 80% of its full capacity. This is an effective way to prevent overheating. When the voltage reaches the predetermined level, the charger switches to constant voltage charging. At this stage, the charger maintains a constant voltage while the charging current gradually decreases as the battery charges for a longer time. Since current is decreasing and voltage is held constant, the internal resistance increases. The constant voltage charging stage prevents overcharging the battery, which reduces its lifespan.

CC-CV charging is a widely used charging method because it provides a fast and

efficient charging process. It protects the battery from damage due to overheating or overcharging. Another possible option is Multistage Constant Current - Constant Voltage (MCC-CV) charging as illustrated in figure 2.5c. This is a charging protocol consisting of several different charging currents with different target voltages. Previous studies show that by using multistage currents, the battery can raise the temperature faster in the initial part of the charging protocol [27]. This might be beneficial while charging at temperatures below the optimal charging temperature to increase the cell temperature, since degradation is larger in these conditions [28].

3

Modelling and Charging Performance Analysis of Batteries

3.1 Battery Modelling

This section highlights the internal behaviour of a battery. It also gives the reader a notion of how lithium ion batteries behave during charge.

3.1.1 Comparison of Battery Models

The battery models described in chapter 2.2.1 will be adopted. In order to get an additional understanding of the differences between the models, figure 3.1 shows the voltage with respect to time when charging with a CC-CV protocol at 1 and 4 C-rate. C-rate indicates how fast a battery charges or discharges relative to its capacity. It represents the relationship between current and battery capacity. A C-rate of 1C means the current is equal to the battery's capacity and charging takes one hour. Higher C-rates indicate faster rates and lower C-rates indicate slower rates. A C-rate of 2 takes 30 minutes to charge the battery. As discussed in the theory above, SPM differs vastly in fast charge current regions compared to the DFN model which is the most precise model and can be seen as a reference in this scenario. The lower sub figures in figure 3.1 shows what parts of the SPM model that causes it to deviate from the DFN model. The majority of errors come from open circuit voltage (OCV) over-potential and electrolyte over-potential. The reason why the OCV over-potential differs between SPM and DFN is likely because OCV expression is nonlinear in some phases of charging. This results in SPM that is simplified to the first order and not capturing the OCV dynamics. There is a longer period of constant voltage in the higher current. The reason for this is because the constant voltage phase is ended by a lower current limit. It takes longer to reach this when starting at a higher current.

3.1.2 SoC Definition

In order to be able to charge to a certain SoC level, a way of estimating SoC is crucial. There are different ways of estimating SoC, for example using voltage mapping. Since this work is based on electrochemical models, a suitable way of measuring the SoC is to measure the lithium ion concentration at the negative

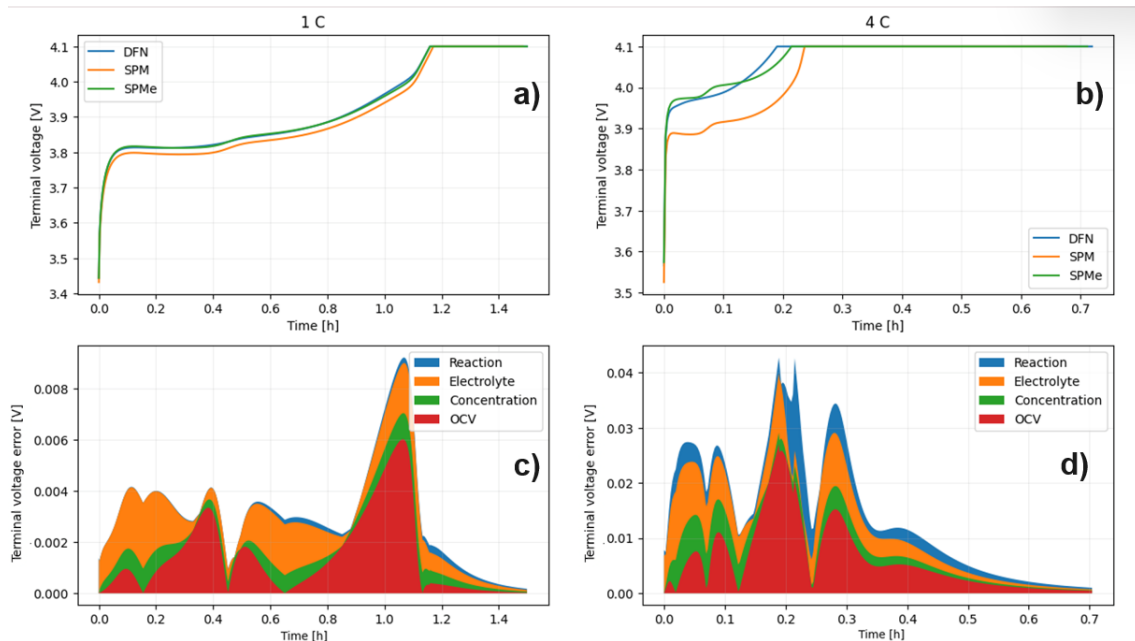


Figure 3.1: A comparison of simulated terminal voltages using various battery models under different charge rates: (a) 1C and (b) 4C. The terminal voltage discrepancies of SPMe compared to DFN under different charge rates are also shown: (c) 1C and (d) 4C.

electrode. The expression for SoC estimation is

$$SoC(t) = \frac{c_{Li^+}(t) - c_{min}}{c_{max} - c_{min}}, \quad (3.1)$$

where $c_{Li^+}(t)$ represents the the averaged concentration of lithium ions in the negative electrode of the battery. c_{min} and c_{max} represent the minimum and maximum averaged concentration of lithium ions in the electrode respectively [27].

3.1.3 Thermal Model

A key variable in creating charging protocols is temperature. The dynamics of lithium ion batteries are heavily dependent on temperature. During charging we will use a built-in PyBaMM model to track the temperature [29, 30].

This work uses [29] and [30] to implement a thermal sub-model in PyBaMM. This model enables the PyBaMM model to compare how different temperature settings in the surrounding conditions affect battery ageing and charging speed. Figure 3.2 illustrates how the average temperature changes within the battery cell during a CC-CV charging protocol. To get an intuition of how the temperature evolves during charge, figure 3.2 shows how the temperature changes during a CC-CV protocol with C-rate 1. The initial temperature is set to the ambient temperature of 20° C. One observation from this figure is that as long as the current is held constant the temperature increases with a decreasing gradient. As soon as the current is decreased the temperature drops and a lower current results in a faster temperature

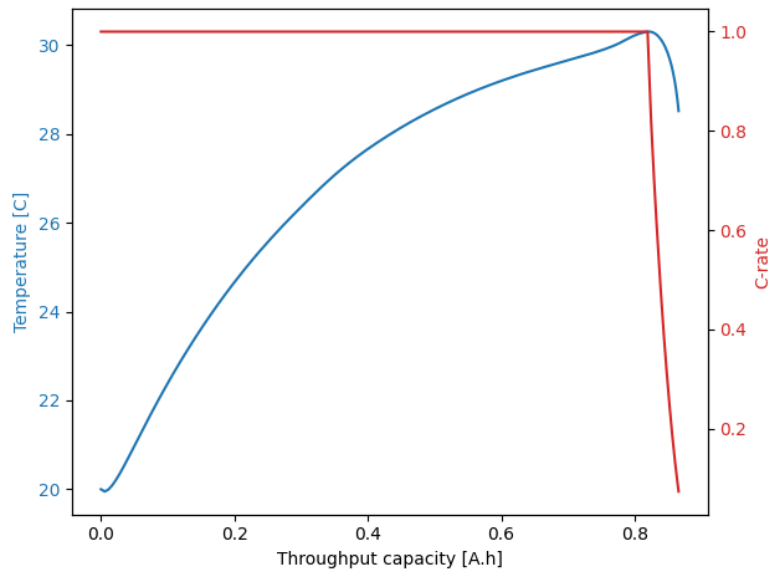


Figure 3.2: Illustration showing how the temperature changes in the lumped thermal model during a CC-CV protocol with C-rate 1.

drop. Depending on how fast and how much the battery is charged, the average

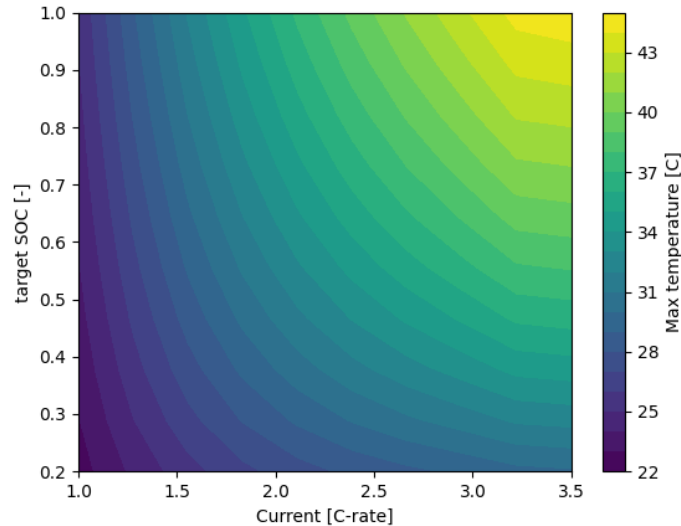


Figure 3.3: Illustration of how the averaged temperature behaves during a CC-CV charge with an initial battery and ambient temperature of 20 °C. The initial SoC is 10 % and the target SoC is shown on the vertical axis.

temperature reached during a charging protocol is different. This is illustrated in figure 3.3 where experiments starting from 10% SoC have been conducted. The average temperature reached after a CC-CV charging protocol decreases with decreasing current and a lower SoC target results in a smaller temperature increment from the initial temperature of 20 °C. Figure 3.4 illustrates how the voltage charge

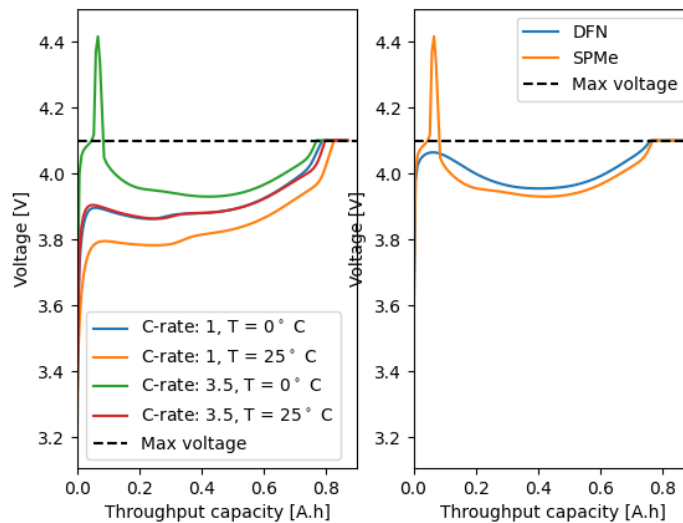


Figure 3.4: The left diagram illustrates the voltage behaviour during CC-CV charging with different currents and ambient temperatures using SPMe. Using a C-rate of 3.5 in 0°C shows a voltage spike exceeding the maximum limit. The right diagram shows how the voltage changes during charging with a C-rate of 3.5 in 0°C with SPMe and DFN. DFN does not display the voltage spike, as shown by SPMe.

curve changes at different temperatures and charging speeds. The left figure illustrates that with an increased charging speed using 3.5 C-rate in cold conditions (0°C), we can achieve the same curve as with a slower charging speed (1 C-rate) and warmer temperature (25°C). The figure also shows that the fluctuations rise above the threshold for the simulation with high C-rate and cold temperature. The right figure shows that this depends on using a SPMe electrochemical model, where identical experiments have been compared between DFN and SPMe models. It also shows that the DFN model doesn't have the same problem. The topic has been discussed further in section 2.2.1.3. For this reason, optimisation will be limited to the regions where this behaviour can be avoided.

3.2 Battery Model Properties

In this section, we will investigate and illustrate the properties of lithium-ion batteries by executing simulations using electrochemical battery models.

3.2.1 Correlations of Key Variables in Charging Process

After seeing how the model behaves in different situations, it was of interest to identify the correlation of model outputs with battery ageing during charge. To this end, experiments with different charging speeds containing 50 full charging cycles were conducted. Figure 3.5 shows a correlation matrix of how some variables correlate to the degradation of the battery during these experiments. Note that temperature

is correlated with diffusivity, which is an important variable in determining charge time. Another point to note is that the total degradation rate is related to the battery SoC. This is a valuable insight as it shows that degradation in the battery is dependent on the battery's energy state. This is one reason fast charging is commonly done in the region of 10 - 80 % SoC.

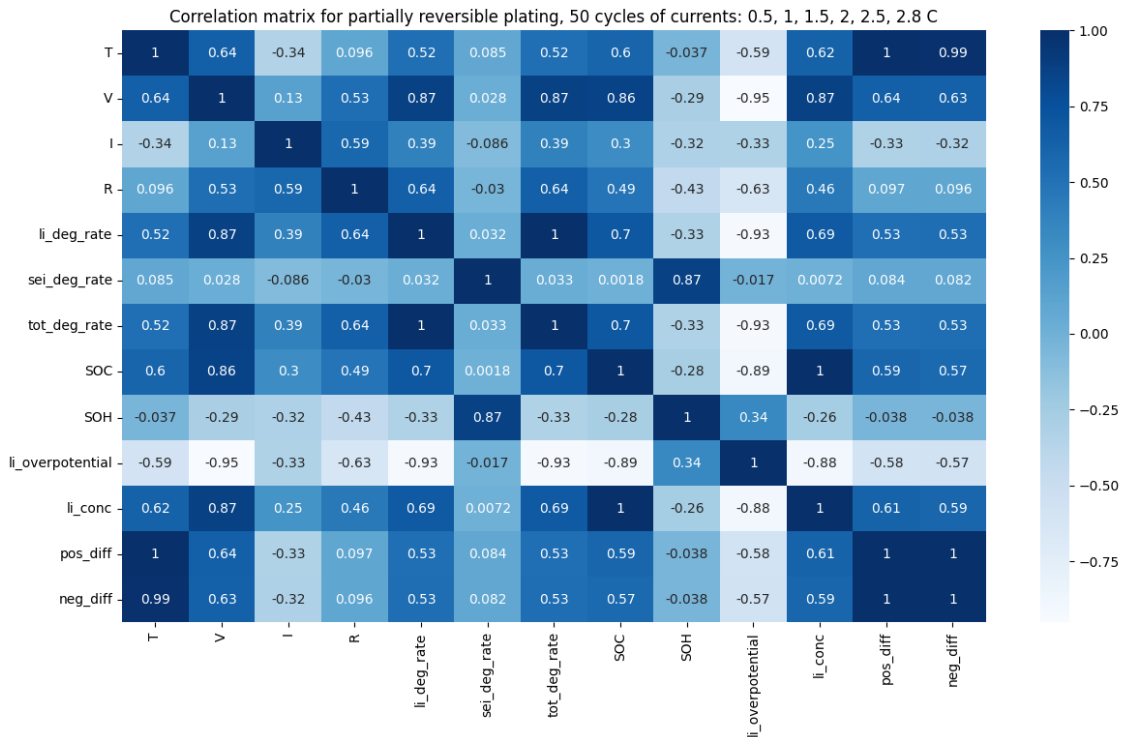


Figure 3.5: Correlation matrix showing the correlation of key variables during a CC-CV charge.

3.2.2 Variables Controlling Charge Time

The time it takes to charge the battery is strongly determined by the current, although the diffusion rate can also matter. As shown in figure 3.5, the temperature and diffusion rate are highly correlated. Figure 3.6 displays the time it takes to charge to a certain SoC. The applied current was a C-rate of 2. The vertical dashed lines shows the transition where the charge protocol transitions from constant current to constant voltage. Temperature does not affect the total charge time in the constant current region, according to the simulation. However in the constant voltage phase, temperature seems to affect the total charge time. Lower ambient temperature increases charge time since it takes longer for the charging current to fade at the constant voltage. Lithium ion propagation is slower at colder temperatures [31], which slows down the propagation of lithium ions. Another observation is that the lowest temperature in the isothermal case has a shorter charge time than at other temperatures. The reason is because the voltage hits the maximum limit of 4.1 V and aborts the charging before it reaches the target SoC, similar to the behaviour found in figure 3.4. The lowest temperature used in figure 3.6 is 5 °C.

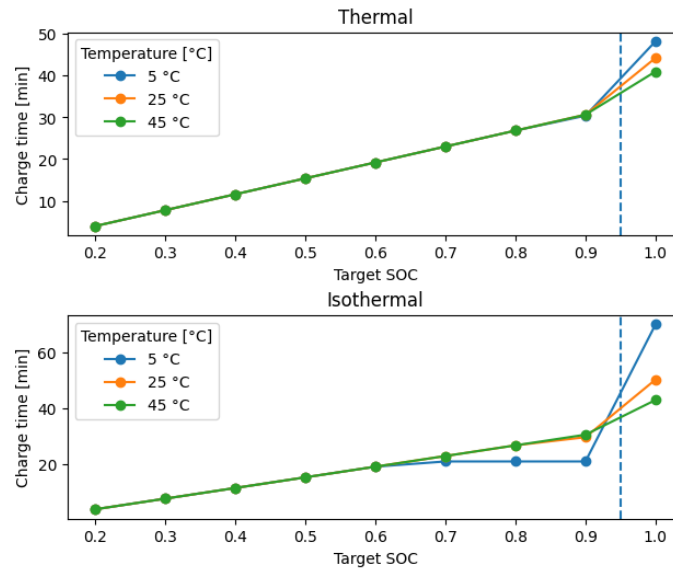


Figure 3.6: Charge time as a function of the target SoC and ambient temperature. There seems to be no difference in charge time at different ambient temperatures in the constant current part of the protocol. The constant voltage part of the protocol is however dependent on temperature where a lower temperature increases charge time.

Numerical instability was observed when simulating charging at high currents and low temperatures using PyBaMM. See figure A.1 in appendix for further analysis of the allowed combinations of currents and temperatures during charge.

3.2.3 Contribution from Different Mechanisms

As mentioned in previous sections, this thesis includes lithium plating, SEI and particle cracking. These mechanisms work differently and are active under different scenarios. In order to comprehend the impact of battery degradation, figure 3.7 demonstrates the capacity loss resulting from various charge currents and ambient temperatures as a function of SoC. In figure 3.7, SEI capacity loss indicates that colder temperatures create less SEI formation. It also appears that higher C-rate creates less SEI. Rather than C-rate, time and temperature influence the formation of the SEI in batteries. Charge times are shortened at higher C rates, resulting in a reduced SEI growth. However, the C-rate indirectly impacts battery performance and SEI stability through factors like temperature and material stress. Particle cracking shows similar trends as SEI when it comes to temperature and current, but the curves have different shapes.

Lithium plating shows the highest amplitude, however the majority of capacity loss occurs in the 80-100 % SoC range, where constant voltage charging is executed. The curve has two plateaus at around 20-30 % SoC and 50-85 % SoC, where the capacity loss changes relative slowly. Figure 3.7 also shows that lithium plating degradation

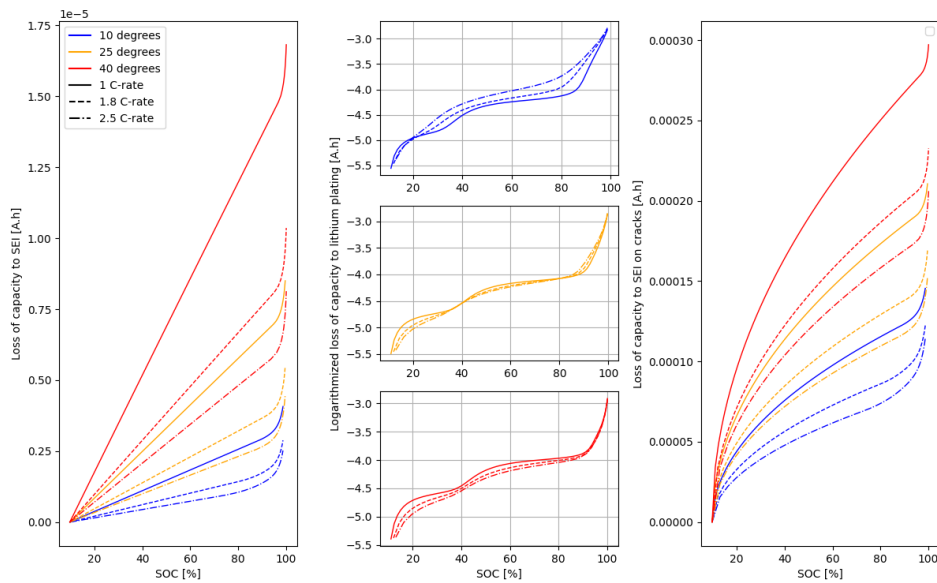


Figure 3.7: Illustration of the degradation resulting from SEI, lithium plating and SEI on cracks during a CC-CV charge of a fresh battery.

is greater at lower temperatures and higher currents. Although not illustrated here, it is noted that lithium stripping occurs during the discharge phase, which resets a substantial portion of the degradation caused by lithium plating.

3.2.4 Long Term Degradation Behaviour

Figure 3.8 illustrates how battery ageing compares for different CC-CV protocols during 500 cycles. As observed in the previous section’s one-cycle experiment, the reactions leading to Solid Electrolyte Interface (SEI) formation are solely dependent on time and temperature, irrespective of the protocol used. Therefore, when plotted against time, the trajectories of various protocols overlap due to the strong time and temperature dependency of SEI formation.

Lithium plating, on the other hand, is triggered by cold temperatures and is influenced by the charging speed of the battery. The occurrence of plating depends on how quickly the battery is charged. During colder temperatures, plating becomes more likely, and charging speed plays a crucial role in its initiation. The extent of plating can impact battery performance and longevity.

The mechanism controlling SEI formation on cracks exhibits fading and current-independent curves at higher temperatures. However, at lower temperatures, exponential growth can be observed during long-term simulations. Lower temperatures tend to trigger more pronounced SEI formation on cracks, which can have implica-

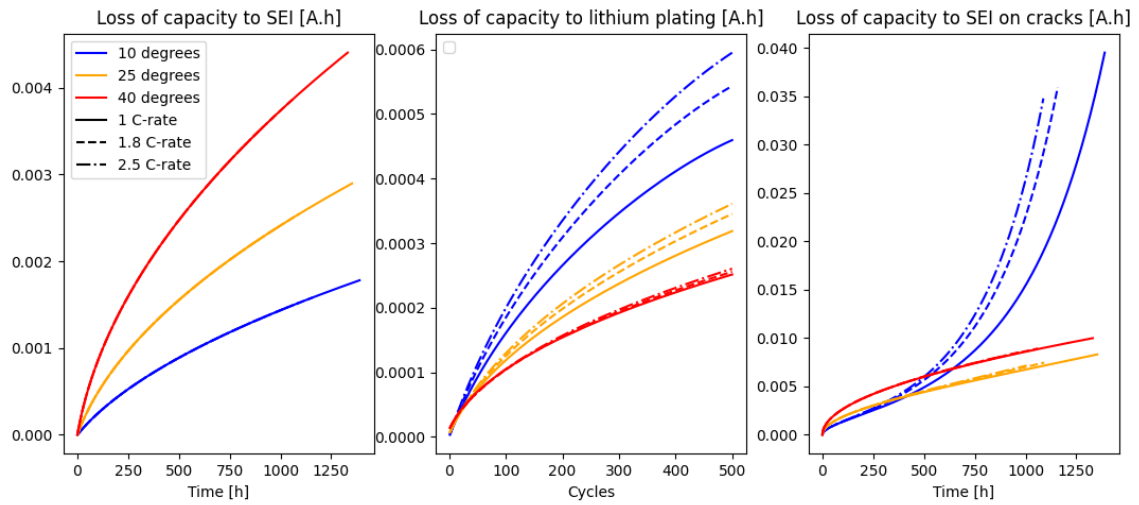


Figure 3.8: Long term battery capacity loss due to SEI, lithium plating and SEI on cracks.

tions for the overall battery ageing process and performance.

This chapter has given information of how our battery and ageing model behaves during charge in various temperatures with different currents. These models will be used when optimising charging protocols which is done in chapter 4.

4

Enhancing Fast Charging Performance through Protocol Optimisation

This chapter focuses on acquiring optimised charging protocols suitable for fast charging while maintaining a healthy battery.

4.1 Problem Formulation

Previous studies have employed various optimisation techniques to design charging protocols. These techniques include Bayesian optimisation, reinforcement learning, and model predictive control [32, 33, 34]. This work uses an evolutionary optimisation algorithm. Evolutionary algorithms have proven useful for being general and global. The objective function is based on the charge time.

4.1.1 Objective Function

As mentioned earlier, the objective is to minimise charge time. This problem might seem trivial; use as high current as possible. There are constraints making the optimisation complex. The entire objective function is stated as

$$\begin{aligned} \min f(SoC, I) &= t_{charge} \\ \text{s.t. } T_{max}(SoC, I) &< 45 \text{ }^\circ\text{C} \\ d(SoC, I) &< d_0. \\ I &= [I_1, I_2, \dots, I_m]^T, \quad I_m \in [0.5C, 3.2C] \\ F(\dot{x}, x, t) &= 0, \quad x \in \mathbb{R}^n, \end{aligned} \tag{4.1}$$

where t_{charge} is a function of SoC and I , which represents the total charge time. As a result of the constraint T_{max} , the maximum average temperature in a battery while charging must be less than $45 \text{ }^\circ\text{C}$. SoC represents the SoC levels where the charging current switch charging current as described in figure 4.1. The $d < d_{max}$ says that the total degradation while charging can not exceed a certain limit d_0 . I represents a vector of m elements, where the allowed currents for m -stage charging protocol are defined in terms of C-rate. The final constraint $F(\dot{x}, x, t)$ states that the differential-algebraic system in PyBaMM needs to follow such a system's dynamics

where x represents the set of variables alluded in chapter 2.

The objective function was chosen as reducing charge time is perhaps the most significant factor when designing the protocol. An alternative objective function based on the sum of charge time and weighted battery degradation was also evaluated. However, we were facing numerical problems when optimising the alternative problem. Moreover, the choice for the weighting was also unintuitive for an engineer.

The variables used to design the charging protocol are the currents and at which SoC levels to switch current if a MCC-CV charging protocol is used. An illustration of how a charging protocol is defined can be seen in figure 4.1. Figure 4.1 illus-

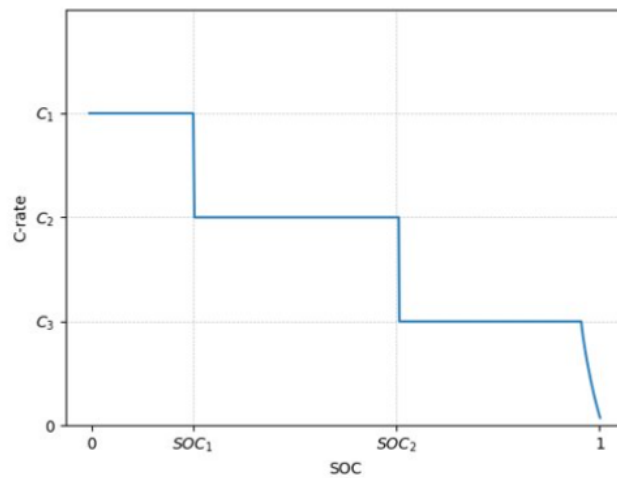


Figure 4.1: Definition of a charging protocol with a 3-stage current. The variables C_1, C_2, C_3 represent the current stages where C_1 is the first current applied. The variables SoC_1, SoC_2 indicate at what SoC the current switches.

trates how a charging protocol is designed. The variables C_1, C_2 and C_3 describe the current stages used when charging. The variables SoC_1 and SoC_2 show the SoC levels at which the current changes. For example SoC_1 indicates the SoC level where the applied current switches from C_1 to C_2 . This illustration shows three different current stages, although any number can be used. The current applied in the region where SoC is close to 1 is non-linear and represents the constant voltage part of the charging profile. Another possible way of modelling a charging protocol would be to set the SoC variables to a fixed value. This would reduce the number of parameters but insights into where to change currents would be lost.

4.2 Optimisation Algorithms

Since this optimisation problem has many variables and different local minima, a global algorithm is required. Since there are quite a few optimisation constraints in our model, the model also needs to incorporate constraints. Evolutionary algorithms are a suitable candidate for meeting these requirements. Evolutionary algorithms use

phenomena from living organisms and nature to converge on a solution and have been applied to various problems. The evolutionary algorithm controls exploration and exploitation on a global scale. The optimisation done in this work was done using an evolutionary algorithm, where the differential evolution optimisation method in the SciPy Python library was utilised.

4.3 Feasible Operating Regions

Since degradation is dependent on both current and temperature, it would be insightful to understand what degradation and charging current regions are acceptable in the objective function. The following two sections will try to understand this and see how current and temperature affect battery ageing.

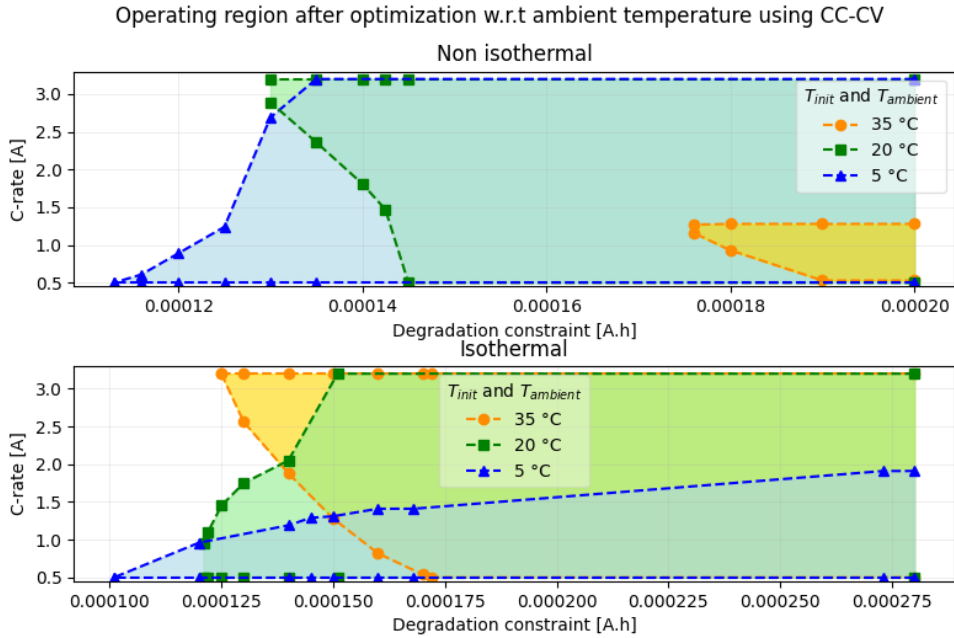


Figure 4.2: Operating regions on a fresh battery where every point is an optimised CC-CV protocol using the objective function presented in (4.1). The x-axis represents the variable d_0 in (4.1), meaning the maximum allowed degradation.

Figure 4.2 shows the operating regions after optimisation for both an isothermal and a non-isothermal case, where one-stage current charging protocol was considered. The C-rates allowed in a 10-80% SoC CC-CV charge protocol as a function of the degradation constraint, d_0 , introduced in the objective function in section 4.1.1 are illustrated. This means that charge protocols with low degradation are situated to the left. The coloured areas show the feasible regions fulfilling the constraints.

As a result of the battery exceeding the 45 °C temperature limit, the current in the 35 °C case is significantly lower than the current in other cases. The reason the region for the warmest temperature is located to the right, meaning the optimisation does not find any solutions for small degradation constraints is because SEI

is dominant at high temperatures. The 35 °C region in the isothermal case has a similar shape but accepts higher currents since the temperature is fixed. The reason why the 35 °C region has the shape where higher currents are accepted where lower are not is because SEI is mostly dependent on temperature and the time the battery is exposed. This means that a higher current makes for a shorter charge time which implies that the battery takes a shorter time to age due to SEI.

The 20 °C regions show different behaviours in isothermal and non-isothermal cases. In the non-isothermal case, higher currents cause less degradation, and in the isothermal case, low currents cause less degradation. The explanation why these differ is because the non-isothermal model heats up to around 45 °C which is in the temperature range where SEI is dominant and results in high degradation. The argument for high current is the same as the case for 35 °C explained above.

The coldest temperature, 5 °C indicates that charging with a lower current gives less degradation. The reason is because lithium plating has a large impact on degradation at that temperature. Lithium plating growth is dependent on the current, which is why there is less degradation at small currents. The current in the isothermal case does not reach the maximum allowed current because the model cannot simulate such high currents in low temperatures.

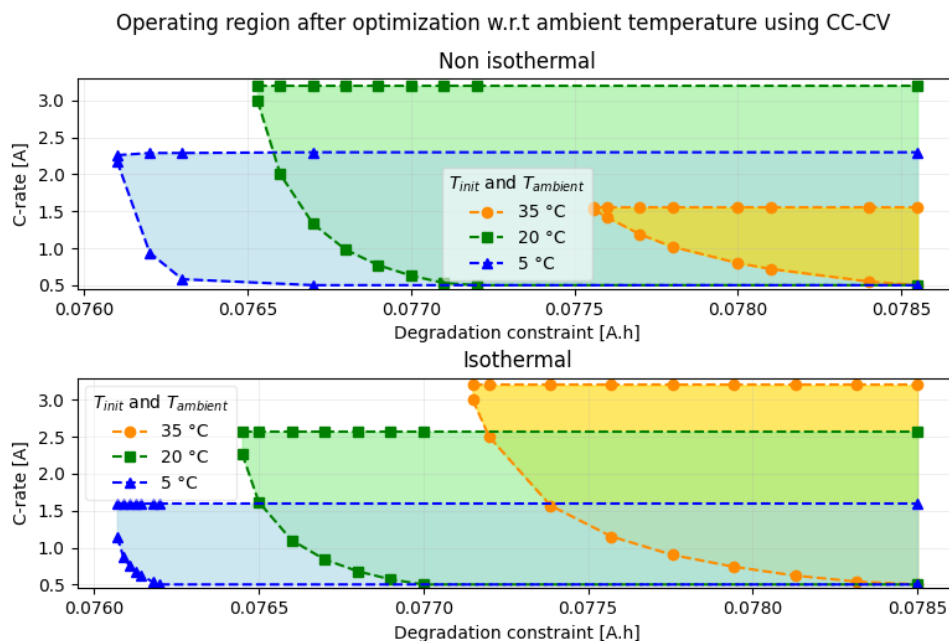


Figure 4.3: Operating region on a seasoned battery where every point is an optimised CC-CV protocol using the objective function presented in (4.1). The horizontal axis represents the variable D in (4.1), meaning the maximum allowed degradation.

To investigate how the charging current feasible regions change as a battery ages, the optimisation problem (4.1) was solved for a seasoned battery with an initial 92% state of health, where SEI, plating and cracking were considered. As shown in figure

4.3, the C-rates are illustrated for CC-CV charging from 10% to 80% SoC. Based on the previous insights from figure 4.2, one observation is that degradation has made SEI growth the lower limit of all regions, independent of ambient temperature. The reason that the 5 °C setting has a lower upper limit than a C-rate of 3.2, for both isothermal and non-isothermal conditions, is due to computational limitations for the SPMe model in PyBaMM.

For the non-isothermal optimisation, the warm simulation is conducted at a temperature of 35 °C, with an upper limit of 45 °C and a lower limit defined by the SEI growth. Both the 5 °C and the 20 °C optimisation regions have the maximum possible current as the upper limit and SEI growth as a lower limit. For the isothermal setting the 20 °C setting has a lower limit than 3.2 C-rate is due to voltage spikes higher than 4.1 V for higher currents, similar to the result presented in figure 3.4. Other than this, regions have lower limits due to SEI growth and upper limits due to maximum possible currents.

All in all, battery degradation in aged batteries is heavily controlled by SEI growth and cracking. This is similar to figure 3.8 where these mechanisms are dominant over lithium plating after long term degradation. The degradation in terms of A.h is also significantly higher compared to figure 4.2.

4.4 Multistage Current Optimisation

After seeing the degradation behaviour of a CC-CV protocol, a natural extension to further investigate charging protocols is utilising multistage current protocols. Optimisation based on evolutionary algorithms was once again used to obtain MCC-CV charging protocols. The objective function used in the optimisation is defined by

$$\begin{aligned}
 \min f(SoC, I) &= d \\
 \text{s.t. } t_{\text{charge},m} &= t_o \\
 T_{\max}(SoC, I) &< 45 \text{ }^\circ\text{C} \\
 I &= [I_1, I_2, \dots, I_m]^T, \quad I_m \in [0.3C, 3.2C] \\
 F(\dot{x}, x, t) &= 0, \quad x \in \mathbb{R}^n,
 \end{aligned} \tag{4.2}$$

where d symbolises the total degradation that was caused in a charging process, $t_{\text{charge},m}$ represents the charge time using m current stages in the charging protocol and t_o represents a desired charge time. SoC represents the SoC levels where the current switch and I contains the current stages that are used while charging. The final constraint $F(\dot{x}, x, t)$ states that the differential-algebraic system in PyBaMM needs to follow such a system's dynamics.

The way this objective function should be interpreted is that the optimiser tries to find a MCC-CV charging protocol that minimises degradation for a specific charge time. Figure 4.4 shows a comparison between charging protocols with different number of currents. Figure 4.4 shows how degradation is affected by the number of cur-

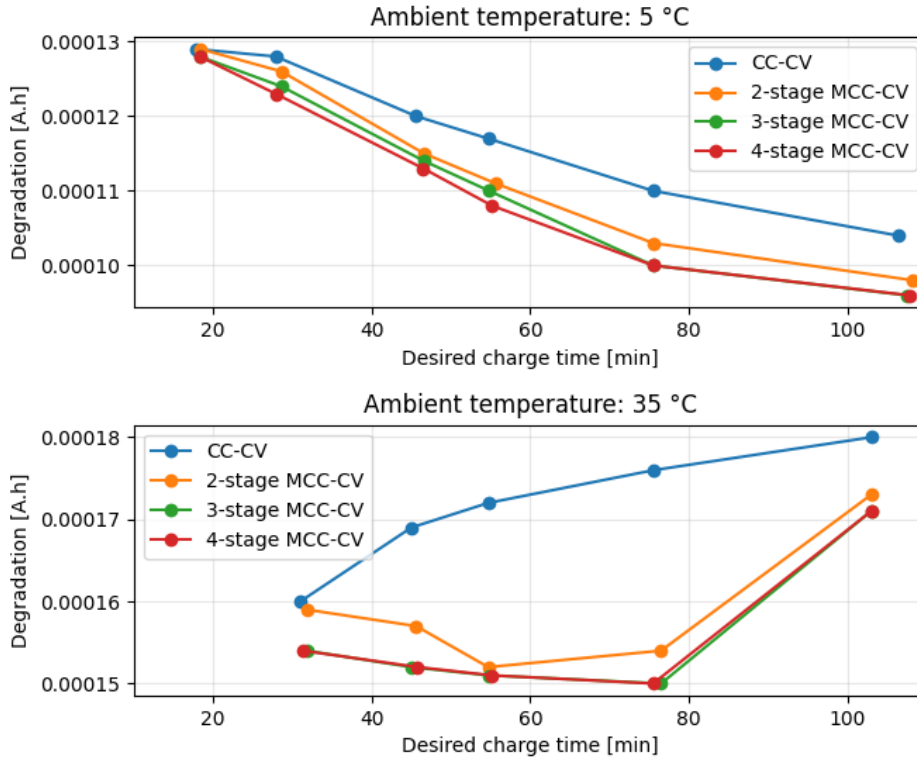


Figure 4.4: Comparison of capacity loss created with respect to the number of current stages and the desired charge time. There seems to be a benefit in terms of degradation from using a 2-stage current in the charging protocol. However, for the lowest possible charge times, multistage charging does not seem beneficial in terms of degradation.

rents in a 10 - 80 % SoC charging protocol as well as the desired charge time. All the protocols have been optimised with the objective function defined in (4.2) by using evolutionary optimisation. Figure 4.4 indicates that lower degradation is achieved by using two or more different current stages in the charging protocol. However, switching from one to two current stages is the most significant change. A change from two to three current stages only results in a slight decrease in degradation, and having more than three or four current stages seems unnecessary. Figure 4.4 also shows a dependency on the desired charge time. The difference between MCC-CV protocols and CC-CV protocols seems to occur in the 40-60 minute charge time range. In contrast, there is not much to gain from charging with multistage currents in 20 minutes. The reason for this is likely because the mean current has a C-rate around 3 during a 20 minute charge time protocol. This forces MCC-CV protocols to have higher C-rates since the maximum allowed C-rate is 3.2. Figure 4.4 also

indicates that optimised MCC-CV protocols are more ageing aware than CC-CV protocols.

4.4.1 Optimised Protocols

According to figure 4.4, a MCC-CV charging protocol can reduce battery ageing during charging. The trend of optimised charging protocols might be worth investigating. The optimisation variables from the 2-stage current charging protocols are shown in table A.1 where C_1 , SoC_1 and C_2 represent the variables defined in figure 4.1. Figure 4.5 illustrates the optimised charging protocol variables using a 2-stage current protocol. At 5 °C ambient temperature, the first current is higher than the second one. The opposite behaviour is shown at 35 °C. Another pattern can be seen in the SoC transition parameter SoC_1 . The current change from C_1 to C_2 is found in the region $[0.59, 0.79]$ for 5 °C ambient temperature and decreases as the charge time increases. The same applies for 35 °C ambient temperature but SoC_1 is found in the region $[0.38, 0.47]$.

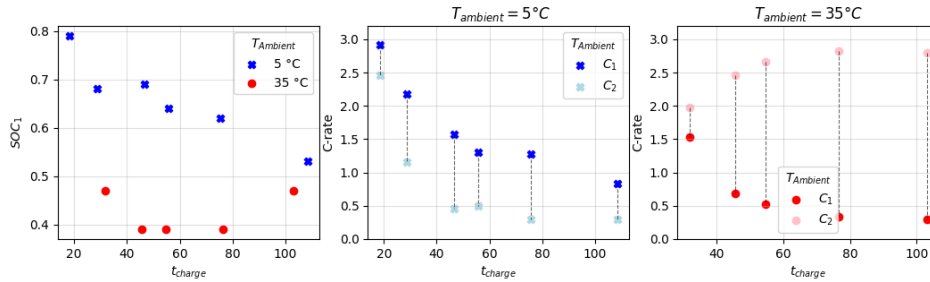


Figure 4.5: Overview of the design of optimised MCC-CV protocols using 2-stage current. The left hand figure shows the SoC where the current switches. The middle figure indicates that the first current is always larger than the second. The right hand figure indicates that the second current is larger than the first one.

4.4.2 Long-Term Behaviour

Figure 4.4 illustrates a significant reduction in degradation for one cycle optimisation while using two currents in a MCC-CV protocol compared to using a one current CC-CV protocol for both 5 and 35 °C ambient settings. Since the objective is to gain insights regarding how the battery lifespan is affected, these comparisons need to be made on a larger timescale. To make sure that the results from figure 4.4 are applicable to these situations, these protocols are compared when running 500 cycles. Figure 4.6 illustrates a 500-cycle degradation comparison between a two-current MCC-CV protocol and a CC-CV protocol in a 5 °C ambient setting. The protocols were selected based on the comparison shown in figure 4.4, which shows the most promising results in terms of degradation reduction when using protocols that take around 75 minutes. SEI and cracking seem to result in a large relative increment, while plating dominates and gives a greater absolute reduction. Figure 3.7 for 5 °C shows that the SEI and cracking degradation mechanisms have higher

4. Enhancing Fast Charging Performance through Protocol Optimisation

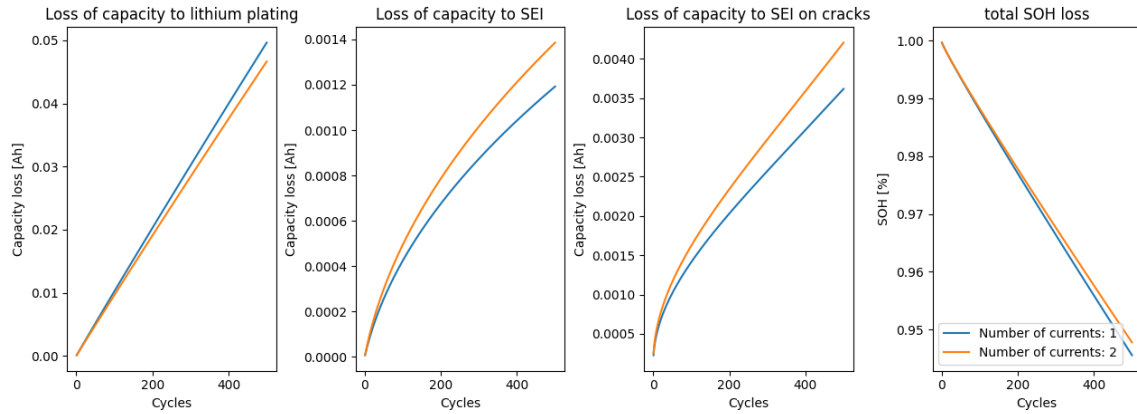


Figure 4.6: Long-term difference between a CC-CV protocol and an optimised two-stage current protocol with an ambient temperature of 5 °C. SEI and cracking seem to be lower for a CC-CV protocol but not for lithium plating which is dominant. This results in the two-stage current protocol generating less capacity loss overall.

degradation at lower currents. In addition, most plating can be avoided up until 80% SoC if the current is held low at the end of the protocol. This can also be found in figure 4.5, which indicates that the optimised two-current protocol uses a higher current followed by a lower one.

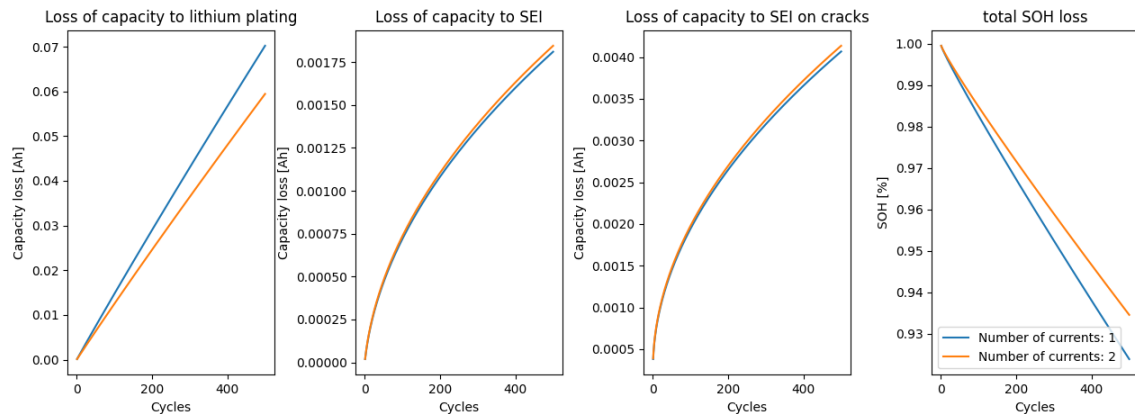


Figure 4.7: Long term difference between a CC-CV protocol and an optimised two-stage current protocol with an ambient temperature of 35 °C. SEI and cracking seem to be similar for CC-CV and the two-stage current protocol but not for lithium plating which is smaller for the two-stage current protocol. This results in the two-stage current protocol generating lower capacity loss overall.

Figure 4.7 presents a 500-cycle degradation comparison between a two-current MCC-CV protocol and a CC-CV protocol in a 35 °C ambient setting. Based on figure 4.4, the protocols selected represent the protocols that take around 55 minutes, as these are the protocols with the best degradation reduction results. It illustrates that the largest reduction seems to be in the lithium plating mechanism. As shown in figure 3.7, lithium plating degrades more rapidly at lower currents compared to higher currents at 40 °C.

Figure 4.2 indicates that the temperature has a substantial effect on both charge time and degradation. Charging with high C-rate can result in high degradation since SEI is dominant in warmer temperatures, and can also risk exceeding the 45 °C temperature limit. The ideal case would be to charge with a high current to reduce charge time and still keep the battery at a reasonable temperature, similar to the isothermal simulations. One approach is to extend the battery model with an active thermal management system (TMS) that can control the temperature of the battery allowing faster charge times which is done in chapter 5 and 6.

5

Modelling of Battery Thermal Management During a Drive Cycle

Fast charging stations are strategically located, often forcing vehicles to drive for a certain period before reaching these stations. This presents an opportunity to optimise the charging process by preparing the vehicle accordingly. This chapter focuses on enhancing charging performance by considering the vehicle's travel route.

The previous chapters lacked a thermal management system (TMS), which is a key feature of this chapter. As mentioned in the previous chapter, controlling the battery temperature would be a powerful tool to improve charging performance. This system will be used to influence the temperature of the battery while it is charging or driving. However the cooling and TMS should not be used excessively since it requires energy.

The objective is to minimise the total travel time from locations A to B while fast charging on the way. Figure 5.1 illustrates the vehicle's route. The given inputs to this problem are the ambient temperature, the motor power output with respect to time and initial conditions. The outputs are thermal management protocols (TMPs) when travelling and a charging protocol. This means that the driving speed is preset before optimisation, which implies that the charge time determines the total travel time. Nevertheless, the driving phases contribute to the total charge time, due to the energy consumed during cooling and heating. Figure 5.1 visualises the events in the route and shows when the different protocols are active.

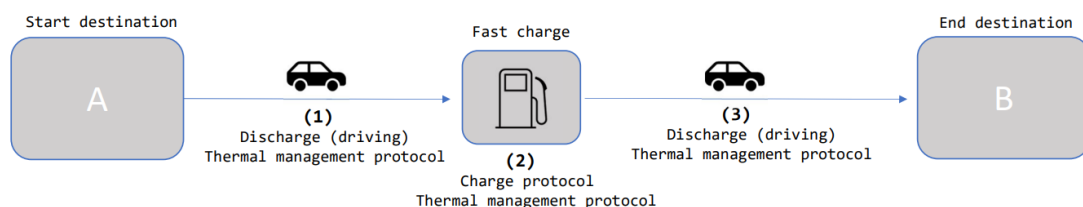


Figure 5.1: Overview of the route. The vehicle starts driving from point A with TMP active. The vehicle is then charged with a charging protocol at a fast charging station and also uses a TMP. Finally the vehicle drives to its end destination at point B while another TMP is active.

5.1 Vehicle-Level Thermal Model Using Coolant Fluid

In order to control the battery temperature in an EV, an accurate thermal model is required. Usually this consists of a coolant circuit where the model captures the behaviour of the coolant propagating between the motor, the climate system, the battery and the condenser. This propagation is made possible by a coolant pump in the circuit. Figure 5.2 illustrates a simplified architecture of a cooling

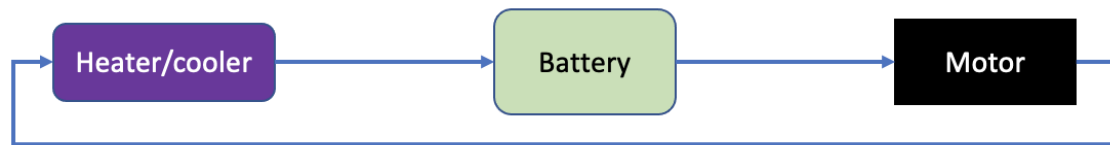


Figure 5.2: Visualisation of the TMS used in an EV. The blue line represents the coolant fluid in the vehicle.

circuit for an EV implementation. The different blocks control how much cooling and heating is created through the different parts of the system. For example, some situations may require more climate cooling than engine heating and vice versa. The different components each represent an interface where a heat transfer is possible with the battery coolant. The interface is either a heat pump or a condenser for the heater/cooler component. The heat generated by the battery coolant can be transferred to the surrounding air or to the battery. The motor interface is not included in the study, but represents heat transfer between the coolant and the motor. The following equations show how this system can be represented in terms of equations while also including a climate system.

$$\begin{aligned}
 q_{br} &= (1 - \eta_b) \cdot |b_{pwr}| \\
 q_{b2bc} &= \eta_{b2bc} \cdot m_{fbc} \cdot c_{p,bc} \cdot (T_b - T_{bc}) \\
 q_{b2a} &= hA_b \cdot (T_b - T_a), a : \text{air} \\
 q_{bc2a} &= hA_{bc} \cdot (T_{bc} - T_a) \\
 q_{bc2mc} &= m_{f_{mc2bc}} \cdot c_{p,bc} \cdot (T_{bc} - T_a) \\
 q_{bc2cc} &= m_{f_{cc2bc}} \cdot c_{p,bc} \cdot (T_{bc} - T_{cc})
 \end{aligned} \tag{5.1}$$

q represents a specific heat exchange where the subscript indicate between what components. All subscripts and variables are presented in the nomenclature list. By incorporating the power demand, it is possible to include the heat loss related to motor efficiency. η_b is the motor efficiency and the equation states that the remaining energy is transferred to the battery.

The remaining heat transfers are related to fluids and interfaces in this system. By using thermal properties in terms of specific heat capacity and heat transfer coefficients, it is possible to account for these behaviours too. All these equations are modelled according to the first law of thermodynamics stating that energy is

conserved in an isolated system. To compute the resulting temperature change, the following equation is used.

$$\begin{aligned}\dot{T}_b &= \frac{1}{m_b c_{p,b}} \cdot (q_{br} - q_{b2bc} - q_{b2a}) \\ \dot{T}_{bc} &= \frac{1}{m_{bc} c_{p,bc}} \cdot (q_{b2bc} - q_{chill} - q_{bc2a} - q_{bc2mc} - q_{bc2cc})\end{aligned}\tag{5.2}$$

The main objective of this study is to determine how the TMS affects the battery and PyBaMM can only control the battery temperature via ambient temperature, so it is preferable to reduce the control of the battery temperature to only the refrigeration circuit. The q_{bc2mc} and q_{bc2cc} terms accounting for the heat transferred between the coolant, motor and climate system will therefore be excluded. However, to include these behaviours, tuning the other parameters to mimic these parts of the model is required. The following equations will therefore be used, where parameters A through D will be found by comparing the model to field test data.

$$\begin{aligned}q_{br} &= (1 - A \cdot \eta_b) \cdot |b_{pwr}| \\ q_{b2a} &= B \cdot hA_b \cdot (T_b - T_a) \\ q_{b2bc} &= C \cdot \eta_{b2bc} \cdot m_{fbc} \cdot c_{p,bc} \cdot (T_b - T_{bc}) \\ q_{bc2a} &= D \cdot hA_{bc} \cdot (T_{bc} - T_a)\end{aligned}\tag{5.3}$$

$$\begin{aligned}\dot{T}_b &= \frac{1}{m_b c_{p,b}} \cdot (q_{br} - q_{b2bc} - q_{b2a}) \\ \dot{T}_{bc} &= \frac{1}{m_{bc} c_{p,bc}} \cdot (q_{b2bc} - q_{chill} - q_{bc2a})\end{aligned}$$

Equation (5.3) includes q_{br} , the heat created from the battery due to losses. q_{b2a} is the heat exchange between battery and air. q_{b2bc} is heat exchange between battery and battery coolant fluid. q_{bc2a} is the heat exchange between battery coolant fluid and air. The battery temperature T_b , and the battery coolant temperature T_{bc} are modelled by a first order differential equation using the heat transfers mentioned above.

5.1.1 Parameter Tuning for Field Test Data

Equation (5.3) introduced the cooling circuit and the corresponding parameters to accurately simulate the EV system behaviour. The parameters A-D must be tuned to get the right signals at each step of the calculation. Field test data is used to tune parameter settings that are relevant in real world conditions. A summary of the field test data is illustrated in table 5.1.

Table 5.1: Summary of the field test data.

Route	Total Distance [km]	Travel Time [hh:mm]	Total Energy [kWh]	Average Ambient Temp [°C]
A-B	153.6	01:45	41	-16
B-C	134.5	01:44	28	-11
C-D	247.6	03:13	56	-9
D-E	153.1	01:54	37	-12
E-F	213.7	02:49	55	-11
F-G	237.9	02:44	56	-8
G-H	112.1	01:21	27	-8
H-I	171.6	02:05	40	-9
	Avg Speed [km/h]	Avg Propulsive Power [kW]	Avg Auxiliary Power [kW]	
A-B	88	17	5	
B-C	77	12	4	
C-D	77	14	3	
D-E	81	16	3	
E-F	76	16	4	
F-G	87	17	3	
G-H	83	17	3	
H-I	82	16	3	

Table 5.1 illustrates a data summary of the field test data used for parameter tuning. There is a small difference in average speed between the different routes and a slightly larger deviation in temperature and energy consumption. Figure 5.3 illustrates how

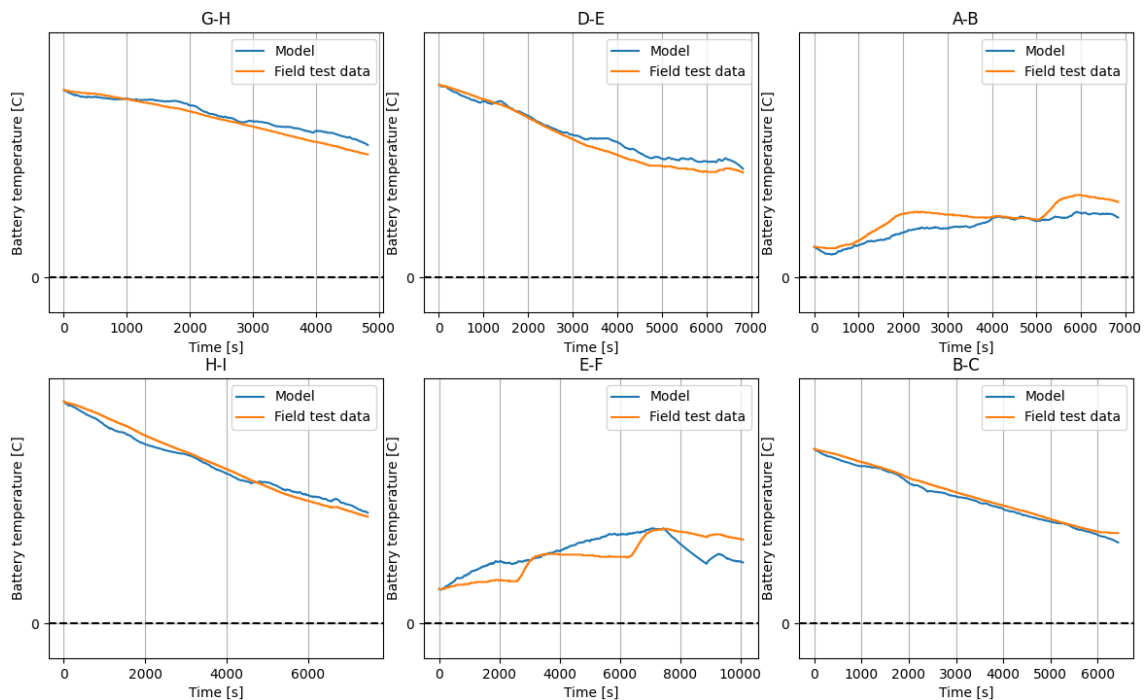


Figure 5.3: Illustration of the results from the parameter tuning of parameters A-D in (5.3) using a set of training routes. Routes A-B and E-F seem to have slightly higher relative error than the others. Their battery temperatures also seem lower compared to the others. The different route locations have been encoded to letters since these are confidential.

parameter tuning affects thermal model accuracy. The untuned model is based

on (5.2). Parameter tuning is an optimisation where the total squared error in battery temperature for all routes is summarised. Regardless of which route leads to a superior outcome, tuning the parameters always yields an improvement over the untuned model. To ensure that the optimisation was not just a specific optimisation

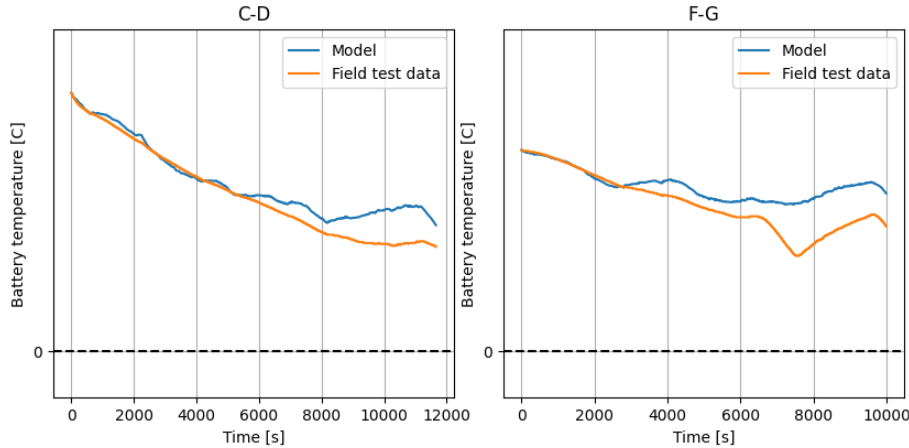


Figure 5.4: Illustration of how the tuned parameters A-D performed on the test dataset. Results seem to be of similar quality to those of the training data in figure 5.3. The different route locations have been encoded into letters since they are confidential. Each letter corresponds to a location.

for the selected routes, two test routes were separated from the dataset to be used as test cases. This verifies that the model can be applied to a more general dataset and not just our data. These are illustrated in figure 5.4. Similar results to figure 5.3 are achieved which indicates that the parameters are general in the sense that they can produce similar accuracy for other routes. Figure 5.5 shows the error histogram categorised by routes and temperature intervals respectively. The errors are caused by differences between the field test data and the result from the thermal model with all routes (test and train) included. See figures 5.3 and 5.4. First observation is that the error is bigger for route G-H. Second observation is that the error decreases with increasing temperatures. Route G-H also seems to have a generally cold battery temperature during the whole drive cycle, so these two ways of illustrating error emphasise the same point. The model gives a smaller error for simulations where the battery temperature is higher.

5.1.2 Model Hierarchy

The ideal approach to optimise the entire route including charging would be to use PyBaMM in the entire modelling process. However this is not feasible due to heavy computational load and long simulation time, even if SPM would have been used. Therefore, segmenting the different driving phases and charging processes into distinct sub-models is essential. This involves creating separate models for the charging phase and the discharge phase, as depicted in figure 5.1. This approach will store the final temperature from one phase and use it as input to the next sub-model. Due to PyBaMM's ability to provide the highest fidelity, it is reasonable to delegate the charging phase to PyBaMM, as it is the most crucial phase of interest

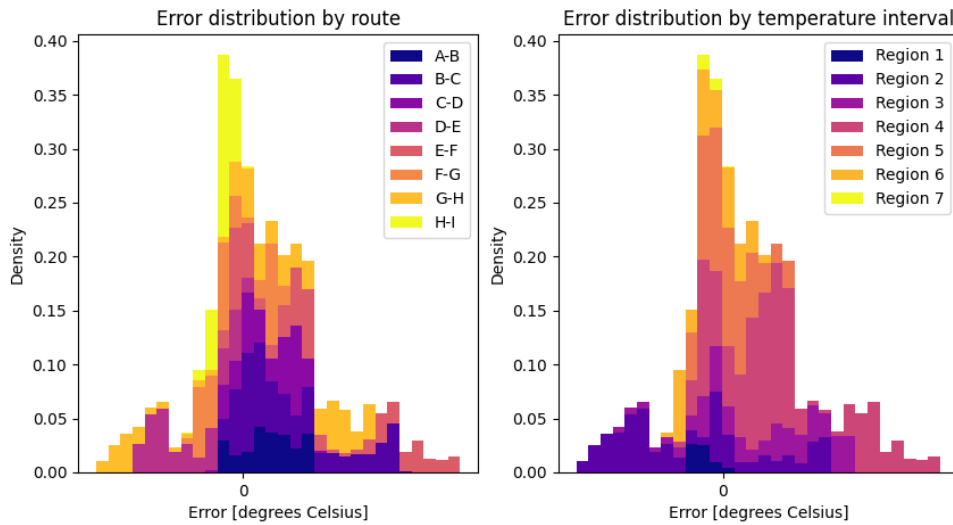


Figure 5.5: Illustration of the absolute error distribution while comparing the tuned thermal model to field test data. As shown in the left image, the data has been categorised by route, with each letter representing a location. The right image shows a histogram where the data is categorised by $5\text{ }^{\circ}\text{C}$ intervals spanning from the lowest possible temperature (interval 1) to the highest possible temperature (interval 7).

in this context. The following two sections will introduce how this model structure can be used for different optimisation approaches.

5.1.2.1 Splitting Model Into Independent Sub-Models

Similar to the industry’s standard practices, this approach focuses on optimising one phase at a time. This effectively diminishes computational burden and reduces simulation times. As a result of the optimisation, a solution will be found that minimises the energy required in the discharge phase and the time required in the charging phase. Figure 5.6 illustrates the optimisation scheme where the black rounded arrows represent the optimisation processes.

5.1.2.2 Full Optimisation Model

It might be beneficial to heat or cool the battery towards the end of the first discharge. This is because the vehicle is about to charge. However, the model in section 5.1.2.1 is not designed for this purpose. As a result, this previous approach causes loss of awareness of the other phases, resembling current industry practice. Figure 5.7 visualises the optimisation process based on the events in the route shown in figure 5.1. The optimisation is done over the full route in one simulation.

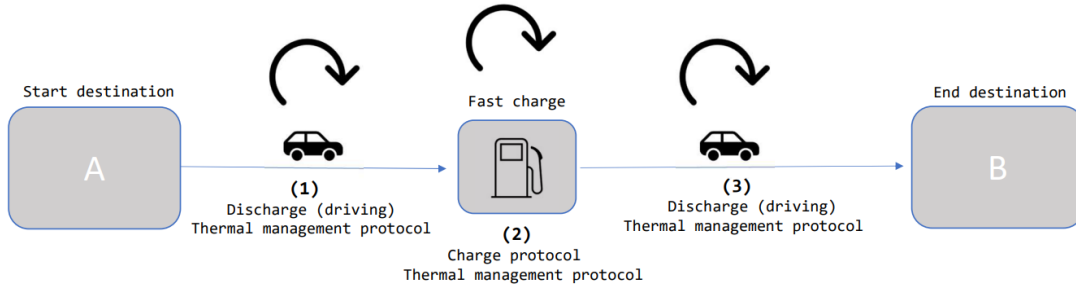


Figure 5.6: Visualisation of the optimisation for the sub-optimisation model. Every phase is optimised independently where every sub model uses fewer parameters than the entire model resulting in faster optimisation convergence.

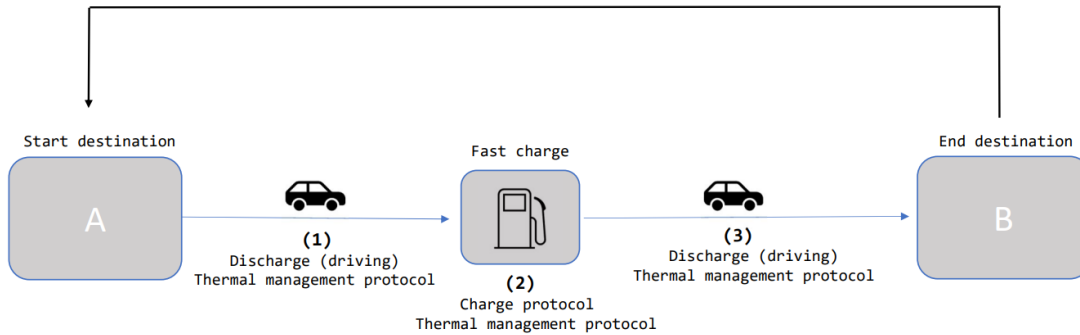


Figure 5.7: Visualisation of the full optimisation model. The model runs through the entire route and evaluates the objective function.

5.2 Thermal Management Protocols

A crucial part of this section is how the battery temperature is controlled. Thermal management protocols (TMPs) will be used to control battery temperature. Depending on whether the vehicle is charging or discharging, the TMPs will differ.

5.2.1 Protocols During Discharge

The structure of a TMP used when the vehicle is discharged is discretised into 50 seconds intervals. An example of a TMP during discharge is shown in figure 5.8. Figure 5.8 shows an example of a TMP used in a discharge process. In this case, the power output is limited to a range between $P_{c,max}$ and $P_{h,max}$. The system cools the battery if the power is in interval $[0, P_{c,max}]$ and heats in interval $[0, P_{h,max}]$. The power output from the TMP is seen in (5.3) as q_{chill} .

5.2.2 Protocols During Charge

Since PyBaMM is used during charging in all models, the heat equations in (5.3) cannot be utilised. Instead, the approach to changing the battery temperature will

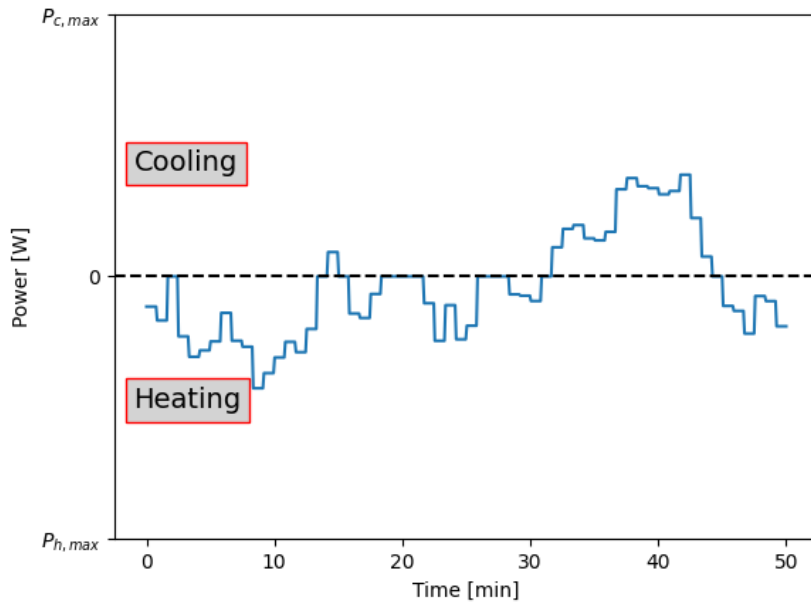


Figure 5.8: The definition of a thermal management protocol (TMP). In (5.3), the power of the TMP is expressed as q_{chill} .

be to change the ambient temperature. The heat transfer coefficient has been tuned from data. PyBaMM has limited freedom in the design of a TMP, making the protocol simpler and not as flexible as TMP during discharge. An example of a TMP is shown in figure 5.9.

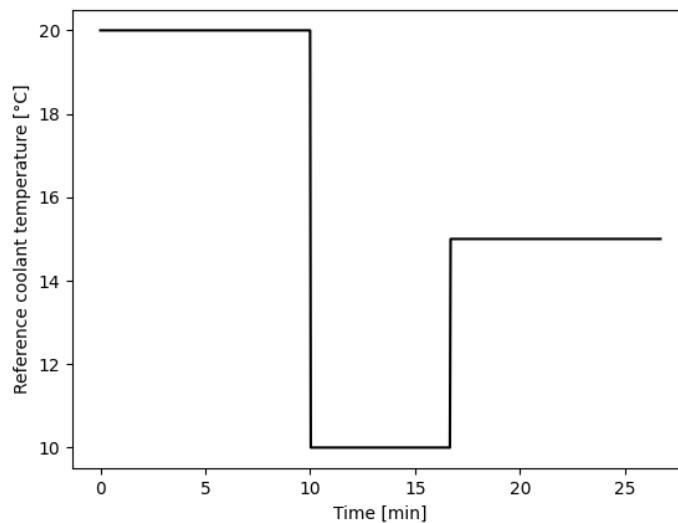


Figure 5.9: Illustration of a TMP during charging in PyBaMM. The reference coolant temperature is controlled through Heaviside's step functions. It changes from 20 to -5 °C after 10 seconds and from -5 to -20 °C after 30 seconds.

The TMP shown in figure 5.9 is designed to incorporate two changes in the reference temperature at different times.

5.2.2.1 Parameter Tuning for Usage in Charging Protocol with PyBaMM

Since the protocol can only control the battery temperature based on the ambient temperature, this temperature needs to change in a similar manner to the battery coolant temperature in the discharge TMP. In order to make the thermal model respond in the same way, the battery heat transfer coefficient needs to be altered. The parameters used assume a perfectly insulated battery without heat leakage. By changing this property faster temperature changes can be produced in the simulations. By using the same train/test split as in section 5.1.1, a similar tuning by this transfer coefficient is conducted. Figure 5.10 illustrates how the optimised tuned

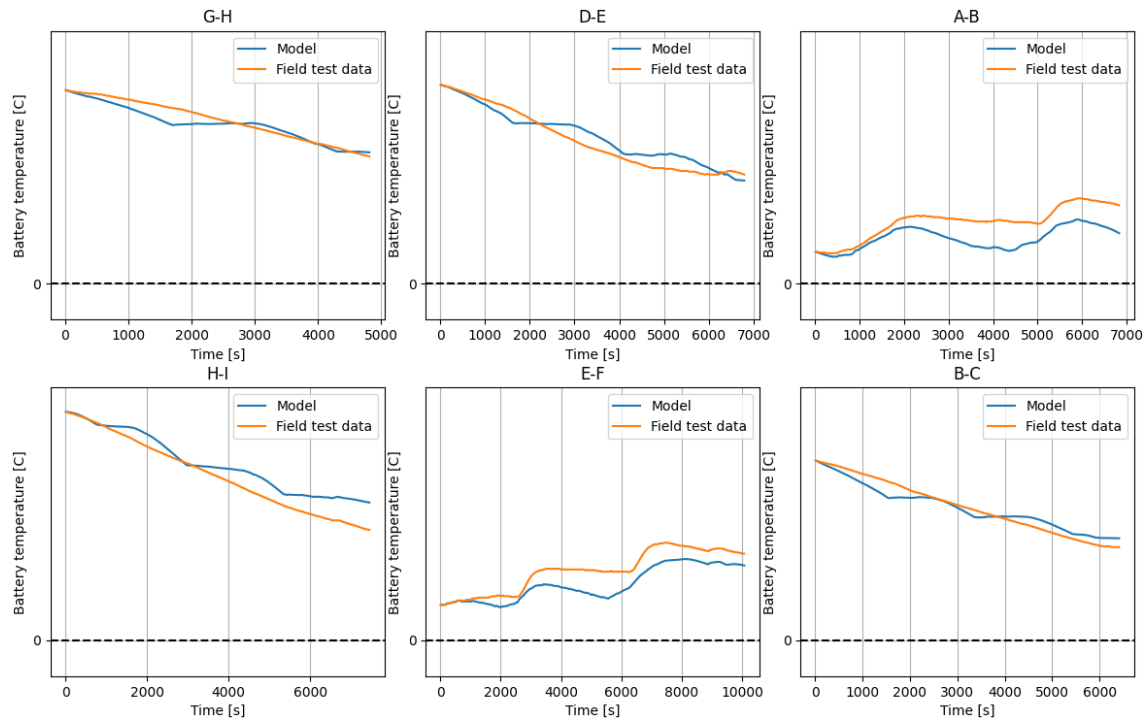


Figure 5.10: Illustration of the results of the parameter tuning of the surface heat transfer coefficient in PyBaMM using a set of training routes. Routes A-B and E-F seem to have slightly higher relative error than the others. Their battery temperatures also seem to be slightly lower compared to the others. This error-temperature trend is similar to the one illustrated in figure 5.3. The different route locations have been encoded to letters since these are confidential. Each letter A-I corresponds to a location.

parameter for the surface heat transfer coefficient from PyBaMM compares to the field test data. The accuracy seems to be a bit lower than figure 5.3, but since a simpler thermal model is used in PyBaMM, in comparison to (5.3), this is expected. To check if the tuning is generally applicable, the same test routes are used. Figure 5.4 shows how parameter tuning was performed for the two selected test routes. It

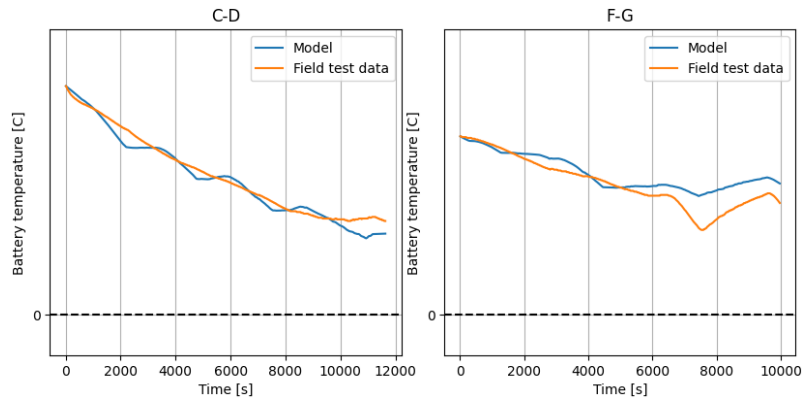


Figure 5.11: Illustration of how the tuned surface heat transfer coefficient from PyBaMM performed on the test dataset. Results seem to be of similar quality to the results from the training data in figure 5.10.

seems like the model’s performance is of similar quality while using these two routes.

This chapter has combined the battery model with a TMS allowing control of battery temperature during a drive cycle. The thermal model was fitted using field test data and tools such as thermal management protocols were introduced. The largest errors for the model can be found when the battery temperature is close to 0 °C Finally two different optimisation methods were presented, where one is aware of the charging process and one is not. The following chapter will present the performance of the two optimisation methods in different temperature settings.

6

Optimising Fast Charging Performance with Thermal Management

By using the charging protocol optimisation presented in chapter 4 and the models for thermal management and optimisation proposed in chapter 5, this chapter explores the optimisation of fast charging performance, where battery thermal management and conditions of a planned route are considered.

6.1 Chapter Overview

Chapter 6.2 discusses phase-wise optimisation, which involves optimising performance under specific conditions. The conditions in this case are two different ambient temperatures, active temperature control, and an empty battery after the trip. Chapter 6.3 discusses full optimisation techniques considering two different ambient temperatures and active temperature control. Chapter 6.4 of the provided information provides a comparison between various factors related to optimisation. These factors are considered in the comparison: full optimisation (see chapter 5.1.2.2), warm ambient temperature, the presence or absence of active temperature control, and maintaining a 50% SoC after driving. These results are evaluated against an industrial baseline.

6.2 Phase-Wise Optimisation

As mentioned in section 5.1.2.1, one optimisation model divides the different phases in the route and optimises them individually. An important observation in this optimisation model is that the vehicle is not aware that a charging phase will begin after the first discharge phase.

6.2.1 Objective Function

The simplified version of the model above is the model shown in figure 5.6, where each phase is optimised separately, reducing the number of optimisation variables.

The objective functions are

$$\begin{aligned}
 (1) \min f_2(q_{\text{chill}}) &= E_1 + a \sum_t |T_b(t) - T_{\text{ref}}| \\
 (2) \min f_1(\text{SoC}, I) &= t_{\text{charge}} \\
 (3) \min f_2(q_{\text{chill}}) &= E_2 + a \sum_t |T_b(t) - T_{\text{ref}}| \\
 \text{s.t. } T_{\text{final,dis1}} &= T_{\text{init,charge}}, \quad T_{\text{final,charge}} = T_{\text{init,dis2}} & (6.1) \\
 E(0) = E_0, \quad E(t_{\text{final,dis1}}) &< E_0, \quad E(t_{\text{end}}) > E_{\text{final}} \\
 T(t) &< 45 \text{ }^\circ\text{C} \\
 I &\in [0.5C, 3.2C] \\
 \begin{cases} F(\dot{x}, x, t) = 0, & x \in \mathbb{R}^n \quad \text{for phase (2)} \\ \dot{y} = h(y), & y \in \mathbb{R}^n \quad \text{for phase (1) and (3)} \end{cases}
 \end{aligned}$$

The first optimisation phase is (1) and the objective is to minimise auxiliary energy during the first driving cycle. E_1 indicates the energy that is required. This is the energy required to heat or cool the battery according to a TMP. The value of T_{ref} represents the desired temperature, and the function penalises battery temperatures that deviate significantly from T_{ref} . The scaling coefficient a is used to adjust the penalty. Variables such as temperature and SoC will be tracked and used as input to the second optimisation (2) where t_{charge} represents the charge time. The second phase optimises the charging process. With the exception of initial values from the charging optimisation, the final optimisation (3) is almost identical to the first (1). E_0 states the initial battery energy level and E_{final} is the energy level at end destination. The final constraints in the function state that the differential-algebraic system in PyBaMM and the ODE in the thermal model need to follow the dynamics of each respective system. x and y are sets of relevant variables during charge and discharge respectively.

6.2.2 Results From Phase-Wise Optimisation

This model optimises every phase independently using PyBaMM to simulate charging. In order to compare the performance of the different optimisation models, different route configurations are presented, such as different ambient temperatures and desired SoC at the final destination. Figure 6.1 gives an overview of the heating and charging protocols along the route. The black dashed lines indicate the charging phase of the route. The upper figure illustrates how the battery and coolant temperature evolves during the route as well as the ambient temperature. The second sub-figure shows the heating and cooling protocols defined in figure 5.8. The figures in the last row show the SoC during each time step of the route. The sub-figure to the right displays the charging protocol. This simulation was done in an environment where the ambient temperature is below $0 \text{ }^\circ\text{C}$, which is considered a cold temperature in a vehicle setting. The algorithm in this simulation is designed to have only enough energy to reach the final destination with only a few percent SoC to spare. Someone who wants to reach the destination as soon as possible with the

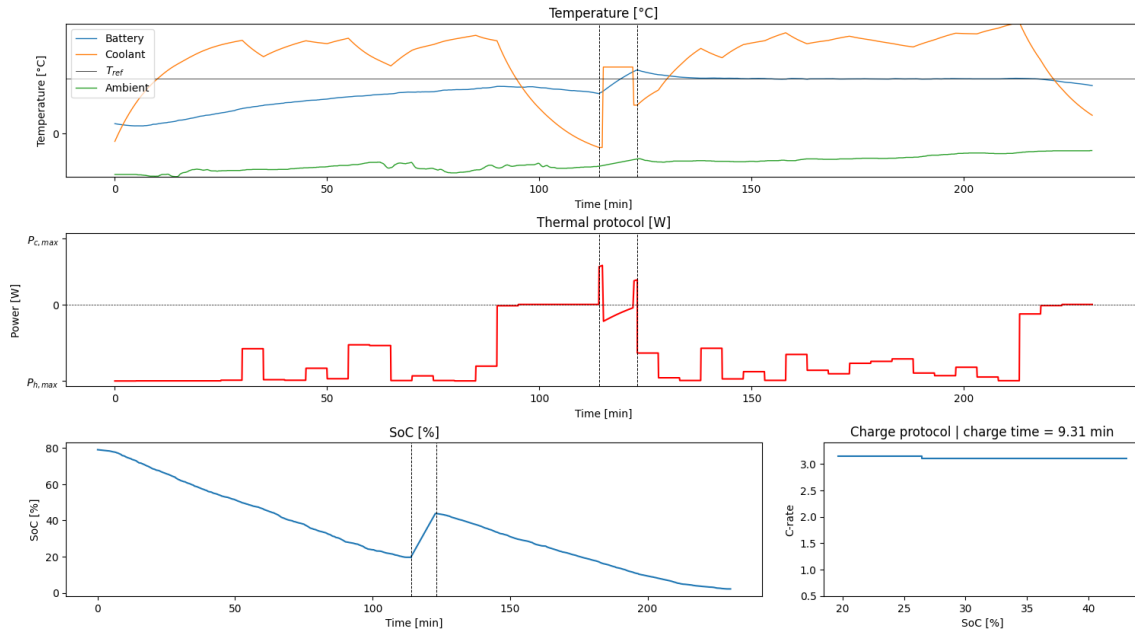


Figure 6.1: Illustration of optimised protocols for cold ambient temperature with phase-wise optimisation and target temperature penalty. Heating is needed to keep the temperature of the battery close to the target temperature. Battery is close to empty when it reaches its destination.

possibility of charging at the destination would fit into this configuration.

The TMPs in figure 6.1 demonstrate consistent heating throughout the entire journey. The reason for this is because the battery temperature is close to the target temperature which is energy consuming when the ambient temperature is cold. A common trend in TMPs is to shut off heating moments before the charging phase. This is because there is a delay between the coolant temperature and the battery temperature. This makes the battery temperature stay at the target temperature even though the coolant temperature decreases.

The charging protocol indicates that a C-rate around 3 is optimal. The best solution in terms of charge time is probably a protocol with 2 currents that both are around the upper C-rate limit of 3.2 since the battery shows no sign of overheating. However, the strong penalty from deviating from the target temperature might result in a reduced charging speed. Figure 6.2 shows the same route overview similar to figure 6.1 with the difference of having a considerably warmer ambient temperature. Like in figure 6.1, the battery temperature stays close to the target temperature in the discharge phase. In order to hold the battery close to the target temperature, the TMP has cooling at almost maximum capacity for most of the time. This is except in the final moments before charging. The optimised charging protocol is almost identical to figure 6.1.

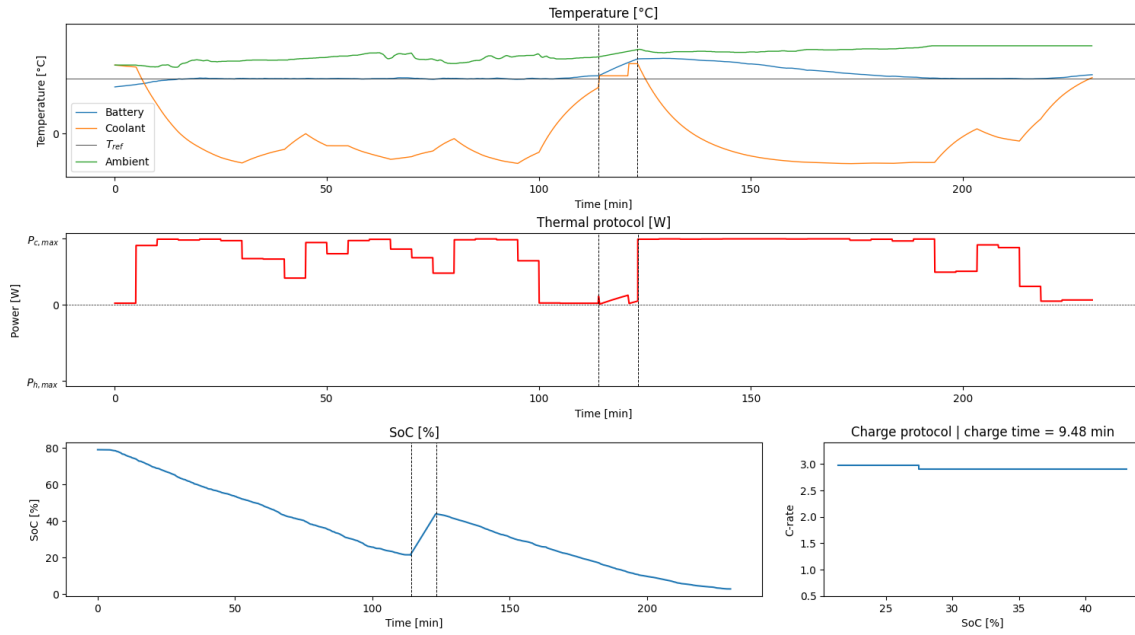


Figure 6.2: Illustration of optimised protocols for warm ambient temperature with phase-wise optimisation and with target temperature penalty. Since the ambient temperature is considerably warmer than the ambient temperature in figure 6.1, cooling has to be done to keep the temperature of the battery close to the target temperature. Battery is close to empty when it reaches its destination.

6.3 Full Optimisation for the Complete Journey

This chapter presents a new optimisation model. This model optimises the entire route in each iteration as discussed in section 5.1.2.2. The main difference from the optimisation model presented above is that the algorithm is aware of the previous and following phases while optimising. The drawback of this model is that it more computationally complex since more optimisation variables are present.

6.3.1 Objective Function

This model uses the heat model in the discharge phase and PyBaMM in the charging phase. The objective function is

$$\begin{aligned}
 \min g(z) &= t_{\text{route}} + b \sum_{t \in t_{\text{discharge}}} |T_b(t) - T_{\text{ref}}| \\
 \text{s.t.} \quad &t_{\text{route}} = t_{\text{dis1}} + t_{\text{charge}} + t_{\text{dis2}} \\
 &T_{\text{final,dis1}} = T_{\text{init,charge}}, \quad T_{\text{final,charge}} = T_{\text{init,dis2}} \\
 &E(0) = E_0, \quad E(t_{\text{final,dis1}}) < E_0, \quad E(t_{\text{end}}) > E_{\text{final}} \\
 &T(t) < 45 \text{ }^\circ\text{C} \\
 &I \in [0.5C, 3.2C] \\
 &G(\dot{z}, z, t) = 0,
 \end{aligned} \tag{6.2}$$

where t_{route} represents the total time the route lasts. The total time is calculated from the sum of the first discharge phase, the charge time and the second discharge time. $T_{\text{final,dis1}}$ denotes the battery temperature at the end of the initial discharge phase, $T_{\text{init,charge}}$ represents the initial battery temperature during charging, and $T_{\text{init,dis2}}$ signifies the initial battery temperature during the second discharge phase. $E(0)$ denotes the initial energy in the battery. E_{final} refers to the desired energy level in the vehicle after the route is complete. The final constraint states that the differential-algebraic system in PyBaMM needs to follow such a system's dynamics.

Something to note is that only t_{charge} varies. The velocity and power output are set, resulting in a fixed discharge time making t_{dis1} and t_{dis2} constant. The way TMPs during discharge affect the objective function is partly to keep the temperature under the limit. The other and more significant way the TMPs during discharge affect the objective function is by how much energy the heating requires. If the TMPs require a lot of energy, the vehicle must charge longer to compensate for the lower energy level upon charge.

6.3.2 Results From Full Optimisation

The results from the full optimisation model are presented in this section.

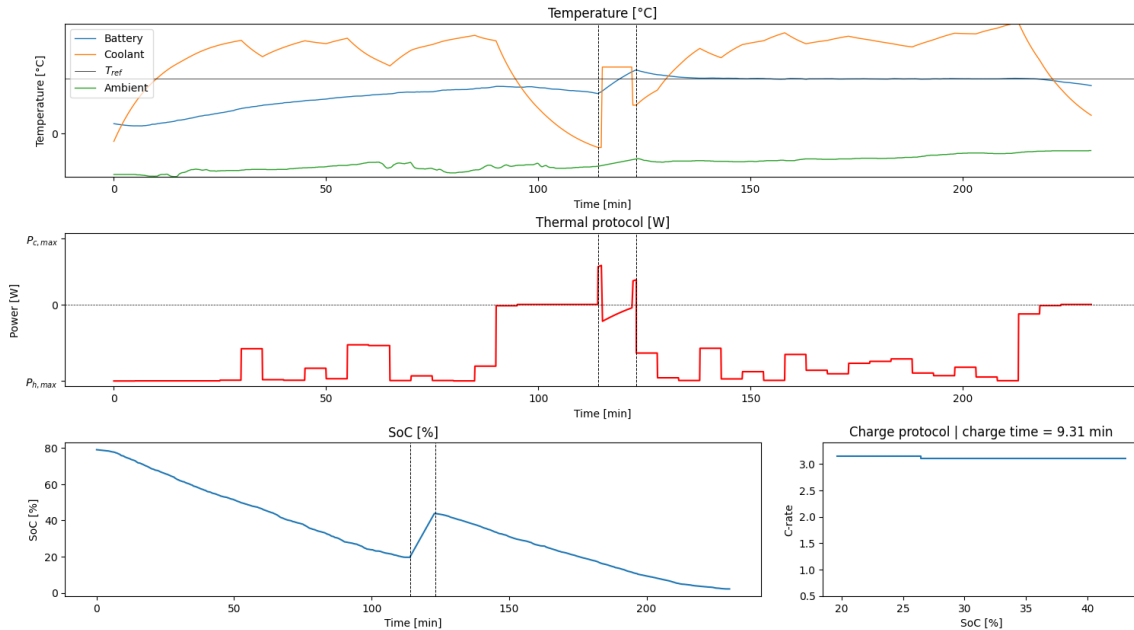


Figure 6.3: Illustration of optimised protocols for cold ambient temperature with full optimisation and the target temperature penalty. Heating is needed to maintain the target temperature. Battery is close to empty when it reaches the destination.

Figure 6.3 shows the result of a full optimisation with a cold ambient temperature, similar to the setup in figure 6.1 with active temperature control. The difference is that the optimisation parameters are found using the full optimisation model. Due to the cold ambient temperature, the TMPs heat the battery the majority of the time to keep it close to the target temperature.

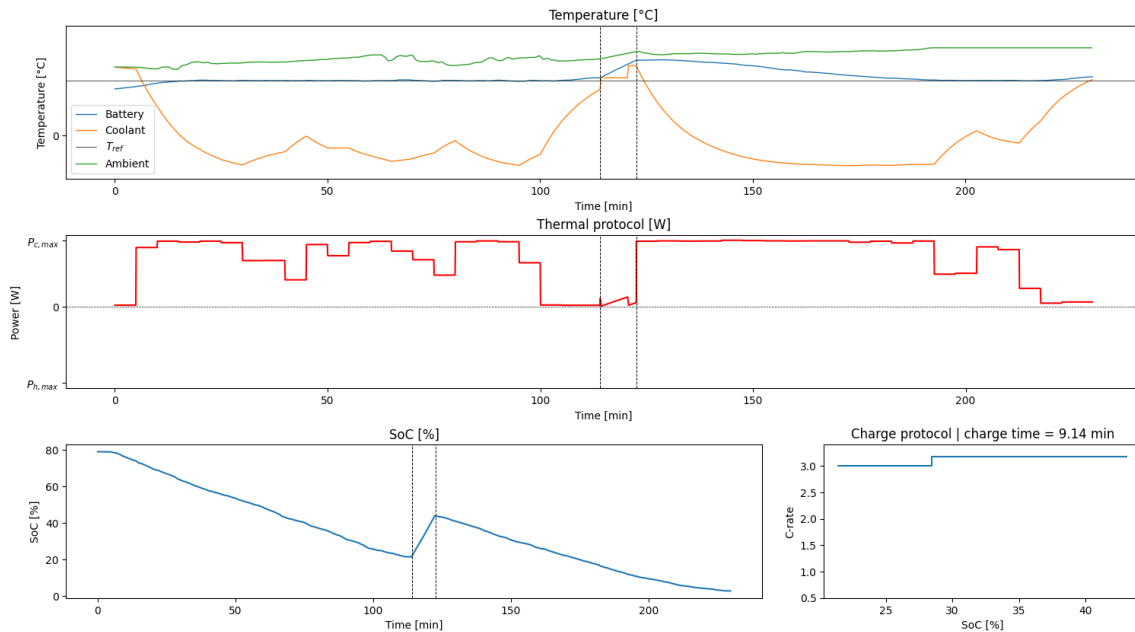


Figure 6.4: Illustration of optimised protocols for a warm ambient temperature with full optimisation and the target temperature penalty. Since the ambient temperature is considerably warmer than the ambient temperature in figure 6.3, cooling has to be done to keep the battery temperature close to the target temperature. SoC is almost empty when it reaches its destination.

Figure 6.4 shows the result of a full optimisation with a warm ambient temperature, similar to the setup in figure 6.2 with active temperature control. According to figure 6.4, cooling is done to keep the battery temperature at the target temperature.

6.4 Comparison and modified objective function

When comparing the different optimisation models it is clear that the TMPs are similarly shaped. Even though the solutions are not identical, they are similar and have the same general shape. The similarity arises from the temperature term inclusion in the objective function. This compels the discharge dynamics to maintain the battery temperature at the target temperature. Letting the discharge phases have similar dynamics simplifies the full optimisation model to only optimise the charging protocol which is how the phase-wise optimisation model is defined.

An approach to further analyse the different optimisation models would be to simplify the objective function. Instead of having a target temperature, this alternative approach would only minimise the route time. This new objective function is identical to the already defined objective functions in (6.2) and (6.1) as long as $a = 0$ in (6.1) and $b = 0$ in (6.2). To extend the analysis, the SoC at the end destination is now set to be 50 %.

To show the effect of the 50% SoC demand on the already used temperature con-

trol a simulation with this requirement is performed in figure 6.5. The differences from optimisation without the 50% SoC requirement seen in figure 6.2 are mainly in the charging protocol and the charge time. An overview of the dynamics with the

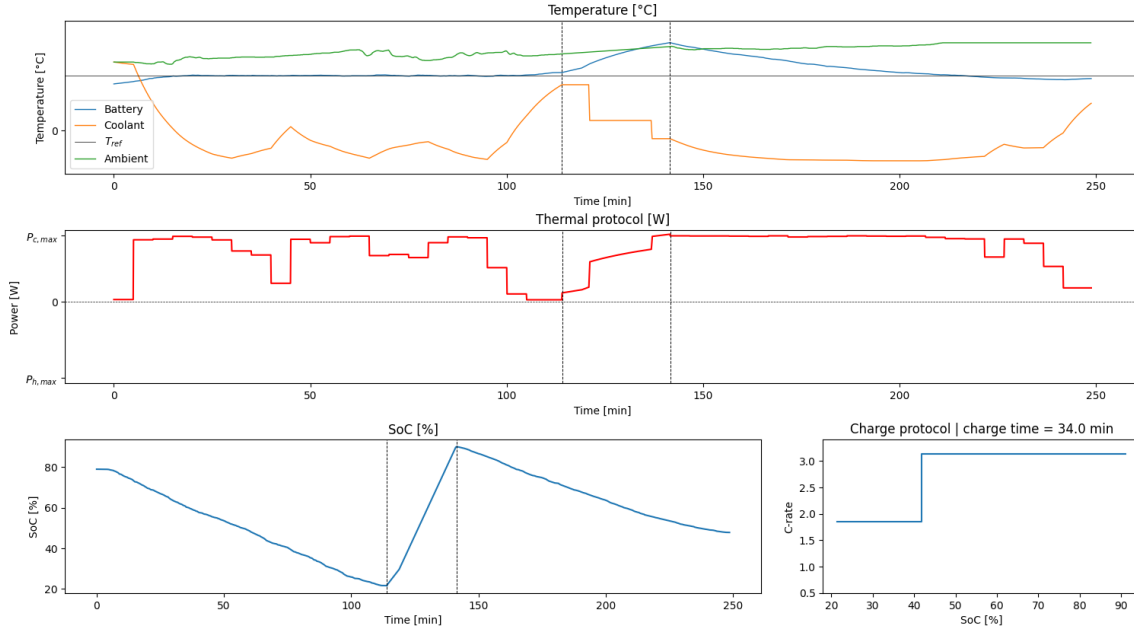


Figure 6.5: Illustration of optimised protocols for warm ambient temperatures with phase-wise optimisation and the target temperature penalty. Since the ambient temperature is warm, cooling is needed to keep the battery temperature close to the target temperature. At the end of the journey, SoC is 50%.

revised objective function can be seen in figure 6.6 and 6.7. Figure 6.6 shows the dynamics of the route temperatures and protocols using the phase-wise optimisation model. This simulation is done at a warm ambient temperature. Since the objective functions only minimises the auxiliary energy in the discharge phases, the battery temperature will be higher than in the previous cases. Starting the charging phase at a high temperature forces charging to be done with lower current even with the cooling system. This results in a longer total travel time. Figure 6.7 shows the temperatures and protocols when using the full optimisation model. This model takes all phases into account at the same time. It ensures that the battery temperature is low enough to charge with high current. This will significantly decrease the charge time and the total route time compared to the charge time in figure 6.6.

The performance of the different optimisation models using the modified objective function varies substantially. Given the revised objective function and specific setup involving warm ambient temperature and the requirement of reaching the end destination with 50% state of charge, it becomes evident that full optimisation is a more appropriate option than phase-wise optimisation. Setting $a = 0$ and $b = 0$ in (6.1) and (6.2) respectively is an extreme case, although the results will converge to the cases above as a and b approach 0.

6. Optimising Fast Charging Performance with Thermal Management

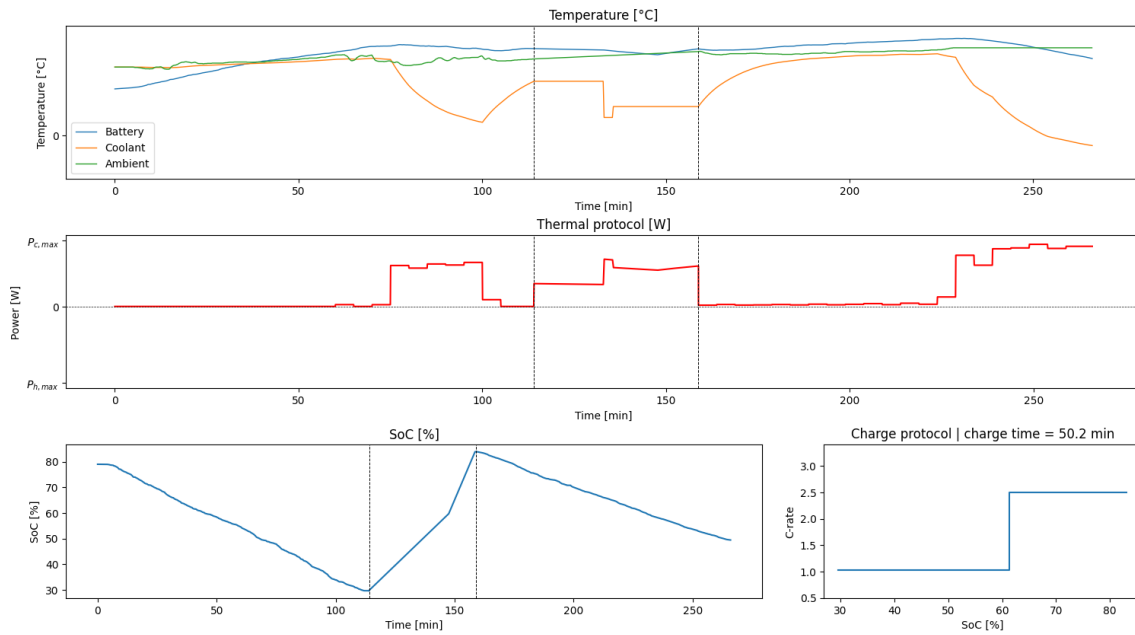


Figure 6.6: Illustration of optimised protocols for warm ambient temperatures with phase-wise optimisation and without the target temperature penalty. The objective function is simplified so that it is only concerned with minimising energy in the discharge phase and the charge time in the charge phase. The SoC is 50% when the EV reaches its destination.

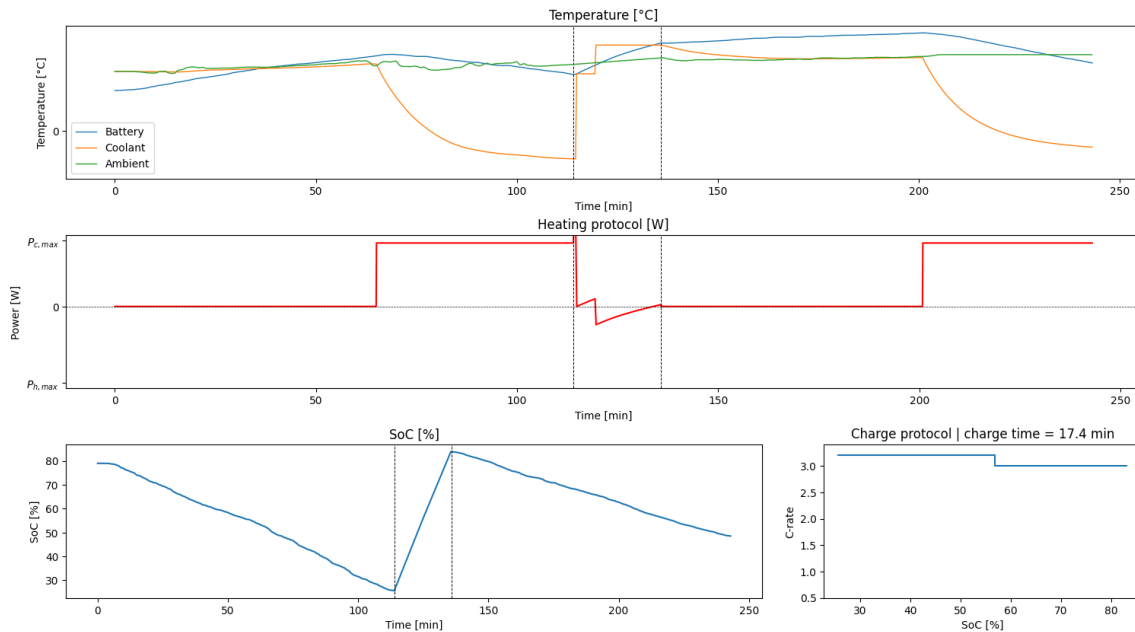


Figure 6.7: Illustration of optimised protocols for a warm ambient temperature with full optimisation and without the target temperature penalty. The objective function is simplified so as to minimise the total travel time. When the EV reaches its destination, the SoC is 50%.

This chapter illustrates the differences between the full optimisation model and the phase-wise optimisation model. The full optimisation model resulted in significant improvements when the battery was prone to overheating. The rest of the report will conclude this thesis and how the work can be continued.

7

Conclusion

7.1 Battery Modelling and Protocol Optimisation

In this work, we adopted battery modelling package, PyBaMM to investigate the optimal fast charging protocol considering battery ageing. A limitation that arose during the work was that PyBaMM could not simulate scenarios at cold temperatures with high currents. Fast charging at cold temperatures can cause excessive battery ageing. This could explain why PyBaMM models crash at certain temperatures with high currents. Figure 3.4 showed that the DFN model does not show a spike in voltage as the SPM_e for extreme cases. The DFN model is more complex and uses fewer assumptions making it a more trustworthy model. However, SPM_e has been used in optimisation throughout the work. The reason is that the DFN model is far too computationally intensive to run in an optimisation setting. Even though SPM_e was faster, it was still heavy on computation time and memory consumption. The optimisation in section 6 was particularly memory-consuming, and it is possible that some of the solutions did not fully converge. The choice of model seems like a trade-off between accuracy and computational speed. For the extreme cases where the SPM_e model crashes, it could be considered more critical to have an accurate model in order to classify which protocols are possible in these extreme situations.

There is a strong correlation between the findings in this work and the objective function chosen. The speed of charging has been a priority which is why the objective function explained in equation 4.1 only minimises charging time with temperature and degradation as constraints. The possibility of using an objective function consisting of the sum of degradation and charging time was explored. However, balancing the different terms was problematic. The objective function defined in equation 4.1 is simple and gives the user control of the degradation significance. The choice of setting the maximum averaged temperature limit to 45 °C in the objective functions is motivated by the fact that the temperature within the battery can vary up to 20 °C. This means that the battery’s warmest point can be 65 °C during charge. At around 80 – 90 °C, the phenomenon thermal runaway can be triggered which can lead to the destruction of the battery [35].

Figure 4.4 indicated that one can achieve lower degradation by charging with a MCC-CV protocol. Optimised two-stage current protocols are temperature dependent. Figure 4.5 indicated that for 5 °C ambient temperature, C_1 should be larger

than C_2 and the current should switch fairly late in the charging process. Similar findings have been found in previous research [27, 36]. However, when the temperature is 35 °C, C_2 is larger than C_1 and the switch was made earlier. One explanation could be that SEI is dominant in warmer environments while lithium plating is dominant in colder temperatures. Further investigation is necessary to fully understand the shape of optimised charging protocols.

Figure 4.4 also indicates that having more current stages than three in a MCC-CV protocol is unnecessary in terms of battery ageing. However, the number of optimisation variables increases with complexity $\mathcal{O}(2n)$ where n is the number of currents in the charging protocol. This meant that having more than three currents in MCC-CV was memory expensive as the optimisation algorithm required longer run times as the optimisation variables increased. The shape of the three staged MCC-CV protocols is similar to the 2 staged MCC-CV protocols with the difference that a third current is active for a very short time. This could likely be a simulation error and has no physical explanation.

7.2 Fast Charging with Thermal Management

The parameter tuning of the thermal model in figure 5.4 shows that the thermal model performs fairly well on field test data. However, figure 6.2 shows that the coolant fluid is colder than 0 °C. This is not quite realistic in the real world. The coolant temperature can be below zero but it is unusual. The reason why the coolant temperature is below 0 °C is because the data is only collected in cold environments. A more diverse data set would probably help train the model with higher accuracy.

What we can see from figure 6.2 and 6.4 is that when the active temperature control tries to keep the battery temperature around the target temperature, the results from the full optimisation and the phase-wise optimisation are of similar performance. The thermal protocols for these two optimisations also indicate battery cooling is needed in both cases. The charging protocols achieve the same charging speed performance. Figure 6.3 and 6.1 shows the optimised solutions for cold ambient temperature using active temperature control with the target temperature. The thermal system has to heat the battery in order for T_{ref} to be reached, but faces no risk of overheating in either case. Like warmer temperatures, the full model and the phase-wise model show similar performance. Since no major differences was found while using the full optimisation for either of the temperatures and the target temperature seemed to be the cause of this, a setup without temperature of penalty was implemented. By conducting this experiment, we could see how the optimisation performed without it.

Two different final SoCs are presented in the simulations from chapter 6. One option is that the SoC is almost empty. This choice makes charging along the route faster. However this assumes that there are charging possibilities at the end destination. What can be observed is that the charging time is quick, sometimes below 10 minutes. This can be desired when the fast charging station is close to the planned

route and makes for convenient charging. In addition, the driver is certain that the vehicle will not be used in the near future before charging again. Setting the SoC at the end destination to 50 % results in a longer charging time. This can exceed the temperature during charging and force the algorithms to cool the battery and charge with a lower current.

According to figure 6.6 and 6.7, when the battery is at risk of leaving the safe operating region and the temperature control is less constrained to match a reference temperature, the full optimisation performs significantly better. Without letting the model remember the outputs from the previous phase and let these decisions affect each other, the charging time can increase significantly. In these cases the charging time is reduced by a factor of ~ 3 . The temperature for the full optimisation is kept lower before charging compared to the phase-wise optimisation, in order to reduce the amount of cooling needed after the charge when the temperature has risen quickly due to fast charging.

The choice of the target temperature defined in equations 6.1 and 6.2 corresponds to what is considered industry standard. However, previous work says batteries work well in the range of 15 – 35 °C for both discharge and charge [37]. This means that keeping the battery at a certain temperature might give the same performance as keeping the battery temperature in the 15 – 35 °C range. Because the temperature is usually within that interval, the T_{ref} term in equations 6.1 and 6.2 might not be necessary. Aside from that, using the target temperature in objective functions usually requires more energy. Figure 6.6 and 6.5 have the exact same configuration with the difference that the optimisation in figure 6.5 uses the target temperature where figure 6.6 does not. The thermal protocols in figure 6.6 consume ~ 3 times less energy than the thermal protocols in figure 6.5.

7.3 Further Work

One aspect to consider in future work is the extension of the existing model to incorporate different choices of routes and charging stations. Currently, the model assumes a predetermined route and charging station. By expanding the model to include various route options and charging station choices, we can better simulate real-world scenarios and evaluate the impact of these choices on charging times, energy consumption, and overall efficiency. This extension could provide valuable insights into optimising route planning and charging station selection for electric vehicles.

To enhance the realism of the model, it would be beneficial to incorporate queues at charging stations. In real-world scenarios, charging stations often experience high demand, leading to waiting times for electric vehicles. By integrating queuing dynamics into the model, we can make the heating protocol aware of queues and the optimisation smarter. Without these types of dynamics, the EV might cool down or heat up before the charger is available and ruin the optimisation. This could identify potential bottlenecks and design strategies to mitigate congestion at charg-

ing stations. This could improve the overall efficiency and reliability of the electric vehicle infrastructure.

Another crucial area for further work is the development of a network for electric vehicles to collaboratively plan their charging activities. By enabling communication and coordination among vehicles, optimisation of charging resources allocation and minimisation of overall energy consumption is possible. This networked approach could involve vehicles sharing information about their anticipated charging needs, current battery levels, and charging station availability. With this information, a centralised or decentralised algorithm could be implemented to determine where and when each vehicle should charge. This algorithm could consider factors such as travel plans, charging station capacities, and overall network load. This collaborative planning approach could lead to more efficient charging infrastructure utilisation, reduced waiting times, and enhanced energy management for the entire electric vehicle network.

The thermal management model used for the driving cycles was simplified to make it similar to the temperature control we could simulate in PyBaMM. The data used for creating the thermal coolant model was also limited to one drive spanning over two days in a fairly consistent climate. In order to make this thermal management system more general it could be interesting to find a way to implement a thermal management system of similar complexity, as the original that was simplified with a full vehicle system, into PyBaMM. This could be used to gain insights into the battery degradation along the entire route, and then all of the optimisation could be done with PyBaMM. It could also be advantageous to utilise a more general data-set to get a more reliable model of the temperatures inside the EV battery.

Bibliography

- [1] Jinhao Meng, Guangzhao Luo, Mattia Ricco, Maciej Swierczynski, Daniel-Ioan Stroe, and Remus Teodorescu. Overview of lithium-ion battery modeling methods for state-of-charge estimation in electrical vehicles. *Applied Sciences*, 8:659, 04 2018.
- [2] Anna Tomaszewska, Zhengyu Chu, Xuning Feng, Simon O’Kane, Xinhua Liu, Jingyi Chen, Chenzhen Ji, Elizabeth Endler, Ruihe Li, Lishuo Liu, Yalun Li, Siqi Zheng, Sebastian Vetterlein, Ming Gao, Jiuyu Du, Michael Parkes, Minggao Ouyang, Monica Marinescu, Gregory Offer, and Billy Wu. Lithium-ion battery fast charging: A review. *eTransportation*, 1:100011, 2019.
- [3] EDF. Benefits of electric cars on the environment. **link**. (accessed: 06.02.2023).
- [4] Volvo cars to be fully electric by 2030. **link**. (accessed: 06.02.2023).
- [5] New York Times. The lithium gold rush: Inside the race to power electric vehicles. **link**. (accessed: 06.02.2023).
- [6] Brendan Mcaleer. Electric car battery life: Everything you need to know. **link**, 10 2022.
- [7] Shropshire star. Electric vehicle owners stuck in long queues at telford services to charge cars. **link**. (accessed: 06.02.2023).
- [8] Peter M. Attia, Aditya Grover, Norman Jin, Kristen A. Severson, Todor M. Markov, Yang-Hung Liao, Michael H. Chen, Bryan Cheong, Nicholas Perkins, Zi Yang, Patrick K. Herring, Muratahan Aykol, Stephen J. Harris, Richard D. Braatz, Stefano Ermon, and William C. Chueh. Closed-loop optimization of fast-charging protocols for batteries with machine learning. *Nature*, 578(7795):397–402, Feb 2020.
- [9] Yiqun Liu, Y. Gene Liao, and Ming-Chia Lai. Temperature variations of a lithium-ion polymer battery cell during electric vehicle driving cycles. In *2021 IEEE Transportation Electrification Conference and Expo (ITEC)*, pages 34–39, 2021.
- [10] E.R. Logan and J.R. Dahn. Electrolyte design for fast-charging li-ion batteries. *Trends in Chemistry*, 2(4):354–366, 2020. Special Issue - Laying Groundwork for the Future.
- [11] Simon E. J. O’Kane, Weilong Ai, Ganesh Madabattula, Diego Alonso-Alvarez, Robert Timms, Valentin Sulzer, Jacqueline Sophie Edge, Billy Wu, Gregory J. Offer, and Monica Marinescu. Lithium-ion battery degradation: how to model it. *Phys. Chem. Chem. Phys.*, 24:7909–7922, 2022.
- [12] Qianqian Liu, C. Du, Bin Shen, Pengjian Zuo, Xinqun Cheng, Yulin Ma, Geping Yin, and Yunzhi Gao. Understanding undesirable anode lithium plating issues in lithium-ion batteries. *RSC Adv.*, 6:88683–88700, 09 2016.

- [13] Thomas Waldmann, Björn-Ingo Hogg, and Margret Wohlfahrt-Mehrens. Li plating as unwanted side reaction in commercial li-ion cells – a review. *Journal of Power Sources*, 384:107–124, 2018.
- [14] Rutooj Deshpande, Mark Verbrugge, Yang-Tse Cheng, John Wang, and Ping Liu. Battery cycle life prediction with coupled chemical degradation and fatigue mechanics. *Journal of the Electrochemical Society*, 159:A1730–A1738, 08 2012.
- [15] Jake Christensen and John Newman. Stress generation and fracture in lithium insertion materials. *Journal of Solid State Electrochemistry*, 10:293–319, 05 2006.
- [16] Jie Li, Kasim Adewuyi, Nima Lotfi, Robert Landers, and Jonghyun Park. A single particle model with chemical/mechanical degradation physics for lithium ion battery state of health (soh) estimation. *Applied Energy*, 212:1178–1190, 02 2018.
- [17] Jiaping Zhou, Bo Xing, and Chunyang Wang. A review of lithium ion batteries electrochemical models for electric vehicles. *E3S Web of Conferences*, 185:04001, 01 2020.
- [18] Scott G. Marquis, Valentin Sulzer, Robert Timms, Colin P. Please, and S. Jon Chapman. An asymptotic derivation of a single particle model with electrolyte. *Journal of The Electrochemical Society*, 166(15):A3693, nov 2019.
- [19] Marc Doyle, Thomas F. Fuller, and John Newman. Modeling of galvanostatic charge and discharge of the lithium/polymer/insertion cell. *Journal of The Electrochemical Society*, 140(6):1526, jun 1993.
- [20] M. Safari, M. Morcrette, A. Teysot, and C. Delacourt. Multimodal physics-based aging model for life prediction of li-ion batteries. *Journal of The Electrochemical Society*, 156(3):A145, dec 2008.
- [21] Kevin N. Wood, Eric Kazyak, Alexander F. Chadwick, Kuan-Hung Chen, Ji-Guang Zhang, Katsuyo Thornton, and Neil P. Dasgupta. Dendrites and pits: Untangling the complex behavior of li metal anodes through operando video microscopy. *ECS Meeting Abstracts*, MA2017-01(5):518, apr 2017.
- [22] Rutooj Deshpande, Mark Verbrugge, Yang-Tse Cheng, John Wang, and Ping Liu. Battery cycle life prediction with coupled chemical degradation and fatigue mechanics. *Journal of The Electrochemical Society*, 159(10):A1730, aug 2012.
- [23] Xiangchun Zhang, Wei Shyy, and Ann Marie Sastry. Numerical simulation of intercalation-induced stress in li-ion battery electrode particles. *Journal of The Electrochemical Society*, 154(10):A910, jul 2007.
- [24] Justin Purewal, John Wang, Jason Graetz, Souren Soukiazian, Harshad Tataria, and Mark Verbrugge. Degradation of lithium ion batteries employing graphite negatives and nickel–cobalt–manganese oxide + spinel manganese oxide positives: Part 2, chemical–mechanical degradation model. *Journal of Power Sources*, 272:1154–1161, 12 2014.
- [25] Valentin Sulzer, Scott Marquis, Robert Timms, Martin Robinson, and S. Chapman. Python battery mathematical modelling (pybamm). *Journal of Open Research Software*, 9, 06 2021.
- [26] Peter Keil and Andreas Jossen. Charging protocols for lithium-ion batteries and their impact on cycle life—an experimental study with different 18650 high-power cells. *Journal of Energy Storage*, 6:125–141, 2016.

-
- [27] Kailong Liu, Changfu Zou, Kang Li, and Torsten Wik. Charging pattern optimization for lithium-ion batteries with an electrothermal-aging model. *IEEE Transactions on Industrial Informatics*, PP:1–1, 08 2018. doi: 10.1109/TII.2018.2866493.
- [28] Battery university. Charging at high and low temperatures. (accessed: 08.02.2023).
- [29] Robert Timms, Scott Marquis, Valentin Sulzer, Colin Please, and S. Chapman. Asymptotic reduction of a lithium-ion pouch cell model. *SIAM Journal on Applied Mathematics*, 81:765–788, 05 2021.
- [30] Scott G Marquis, Robert Timms, Valentin Sulzer, Colin P Please, and S. Jon Chapman. A suite of reduced-order models of a single-layer lithium-ion pouch cell. *Journal of The Electrochemical Society*, 167(14):140513, oct 2020.
- [31] Yutaka Motoaki, Wenqi Yi, and Shawn Salisbury. Empirical analysis of electric vehicle fast charging under cold temperatures. *Energy Policy*, 122:162–168, 2018.
- [32] Benben Jiang, Marc D. Berliner, Kun Lai, Patrick A. Asinger, Hongbo Zhao, Patrick K. Herring, Martin Z. Bazant, and Richard D. Braatz. Fast charging design for lithium-ion batteries via bayesian optimization. *Applied Energy*, 307:118244, 2022.
- [33] Changfu Zou, Chris Manzie, and Dragan Nešić. Model predictive control for lithium-ion battery optimal charging. *IEEE/ASME Transactions on Mechatronics*, 23(2):947–957, 2018.
- [34] Saehong Park, Andrea Pozzi, Michael Whitmeyer, Hector Perez, Aaron Kandel, Geumbee Kim, Yohwan Choi, Won Tae Joe, Davide M. Raimondo, and Scott Moura. A deep reinforcement learning framework for fast charging of li-ion batteries. *IEEE Transactions on Transportation Electrification*, 8(2):2770–2784, 2022.
- [35] Manh-Kien Tran, Anosh Mevawalla, Attar Aziz, Satyam Panchal, Yi Xie, and Michael Fowler. A review of lithium-ion battery thermal runaway modeling and diagnosis approaches. *Processes*, 10(6), 2022.
- [36] Saehong Park, Andrea Pozzi, Michael Whitmeyer, Hector Perez, Aaron Kandel, Geumbee Kim, Yohwan Choi, Won Tae Joe, Davide M. Raimondo, and Scott Moura. A deep reinforcement learning framework for fast charging of li-ion batteries. *IEEE Transactions on Transportation Electrification*, 8(2):2770–2784, 2022.
- [37] Daberechi David Agwu, Felix Opara, Nkwachukwu Chukwuchekwa, Damian Dike, and Lazarus Uzoechi. Review of comparative battery energy storage systems (bess) for energy storage applications in tropical environments. *Batteries*, 09 2018.

A

Appendix 1

Table A.1: Table of the two-stage charge protocol with respect to charging time and ambient temperature. The variables C_1 , SoC_1 , C_2 are described in figure 4.1.

t_{charge}	T_{amb}	C_1	SoC_1	C_2
18.37	5	2.92	0.79	2.46
28.6	5	2.18	0.68	1.16
46.5	5	1.56	0.69	0.46
55.6	5	1.31	0.64	0.51
76.7	5	1.26	0.62	0.30
108.3	5	0.83	0.53	0.30
31.8	35	1.53	0.47	1.96
45.6	35	0.68	0.38	2.47
55.5	35	0.52	0.39	2.66
76.6	35	0.34	0.38	2.83
103	35	0.3	0.46	2.82

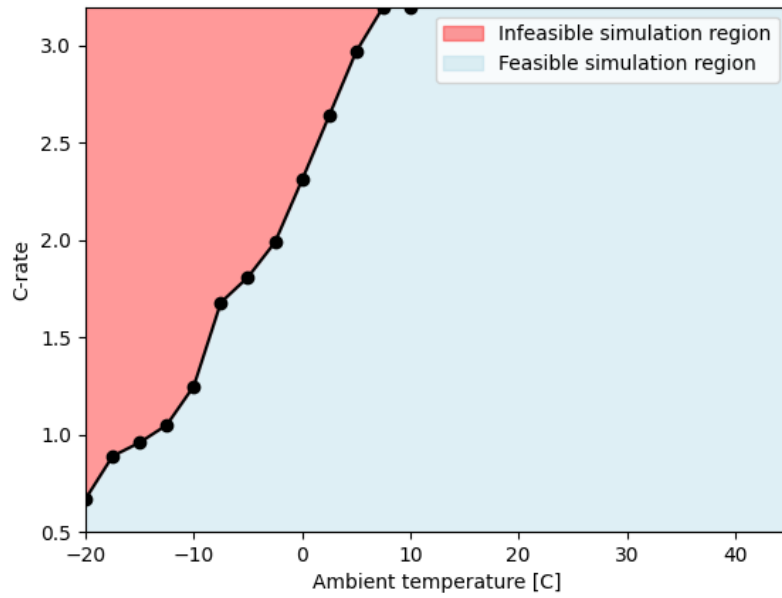


Figure A.1: Operating region for PyBaMM. Numerical instability was observed when simulating charging at high current in cold environments using PyBaMM. During charging, the temperature is fixed in this simulation using a non-isothermal model. If an isothermal model were used, the boundary would be pushed to higher temperatures.

DEPARTMENT OF ELECTRICAL ENGINEERING
CHALMERS UNIVERSITY OF TECHNOLOGY
Gothenburg, Sweden
www.chalmers.se



CHALMERS
UNIVERSITY OF TECHNOLOGY